

Hydroxide-Bridged Five-Coordinate Dy^{III} Single-Molecule Magnet Exhibiting the Record Thermal Relaxation Barrier of Magnetization among Lanthanide-only Dimers

Jin Xiong, ^a Hai-Yan Ding, ^b Yin-Shan Meng, ^a Chen Gao, ^a Xue-Jing Zhang, ^c Zhao-Sha Meng, ^a Yi-Quan Zhang, ^b Wei Shi, ^c Bing-Wu Wang ^{a*} and Song Gao ^{a*}

Supporting Information

I. Synthetic procedures	4
Scheme S1. The synthesis method of complex 1-4	4
II. Structure	5
Table S1. Crystallographic data and structure refinements of Compound 1 and 2	6
Table S2. The CShM's values of the first coordination sphere of compound 1 and 2 , referring to all standard 5 vertices polyhedrons	6
Figure S1. Powder XRD patterns of compound 1-3 and simulated patterns of 1 and 2	7
Figure S2. FT-IR spectra of compound 1-4 and Dy(DBP) ₃ at the range of 400~4000 cm ⁻¹	7
III. Magnetism	8
Figure S3. Temperature dependence of $\chi_M T$ and χ_M^{-1} for a polycrystalline sample of 1	8
Figure S4. Plots of the reduced magnetization M vs H/T at the temperatures of 2 K, 3 K, 5 K, 8 K and 10 K for a polycrystalline sample of 1	9
Figure S5. Plots of zero-field-cooled magnetization (ZFCM) and field-cooled magnetization (FCM) for a polycrystalline sample of 1 under 10 Oe, 50 Oe, 2500 Oe and 10000 Oe.	9
Figure S6. Temperature dependence of $\chi_M T$ and χ_M^{-1} for a polycrystalline sample of 3 . (χ_M was divided by the Dy ratio.)	10
Figure S7. Plots of zero-field-cooled magnetization (ZFCM) and field-cooled magnetization (FCM) for a polycrystalline sample of 3 under 50 Oe and 2500 Oe	10
Figure S8. Temperature dependence of $\chi_M T$ and χ_M^{-1} for a polycrystalline sample of 4	11
.....	11
Figure S9. Plots of the reduced magnetization M vs H/T at the temperatures of 2 K, 3 K, 5 K, 8 K and 10 K for a polycrystalline sample of 4 . Insert: plots of M vs H	11
Figure S10. The first derivative of magnetization (dM/dH) of complex 1 versus magnetic field for the curves measured at 2 K at scan rate of 200 Oe/s, sweep mode	12
Figure S11. The first derivative of magnetization (dM/dH) of complex 1 versus magnetic field for the curves measured at different temperature at scan rate of 200 Oe/s, sweep mode	12
Figure S12. The first derivative of magnetization (dM/dH) of complex 3 versus magnetic field for the curves measured at different temperature at scan rate of 200 Oe/s, sweep mode	13
Figure S13. Plots of magnetic field dependent in-phase (χ') and out-of-phase (χ'') components of ac susceptibility (100~10000 Hz) of 1 at 2 K	13

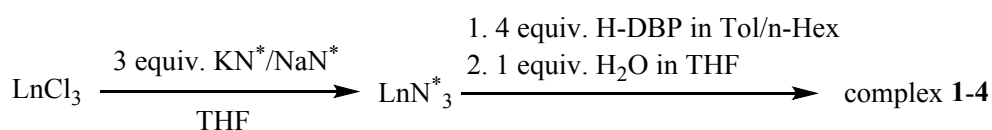
Figure S14. Plots of temperature dependent in-phase (χ') and out-of-phase (χ'') components of ac susceptibility (100~10000 Hz) of 1 under zero static field.	14
Figure S15. Plots of frequency dependent out-of-phase (χ'') component of ac susceptibility (100~10000 Hz) of 1 at zero static field.	14
Figure S16. Plots of frequency dependent in-phase (χ') component of ac susceptibility (100~10000 Hz) of 1 at zero static field.	15
Figure S17. Argand plots of 1 between 34 K and 50 K from the data at Figure S10 at zero static field.	15
Figure S18. Plots of temperature dependent in-phase (χ') and out-of-phase (χ'') components of ac susceptibility (1~1000 Hz) of 1 at zero static field.	16
Figure S19. Plots of frequency dependent out-of-phase (χ'') component of ac susceptibility (1~1000 Hz) of 1 at zero static field.	16
Figure S20. Plots of frequency dependent in-phase (χ') component of ac susceptibility (1~1000 Hz) of 1 at zero static field.	17
Figure S21. Argand plots of 1 between 12 K and 36 K from the data at Figure S14 at zero static field.	17
Table S3. Fitting parameters of 1 at zero static field.	17
Figure S22. Plots of temperature dependent in-phase (χ') and out-of-phase (χ'') components of ac susceptibility (100~10000 Hz) of 1 at 2500 Oe static field.	19
Figure S23. Plots of frequency dependent out-of-phase (χ'') component of ac susceptibility (100~10000 Hz) of 1 at 2500 Oe static field.	19
Figure S24. Plots of frequency dependent in-phase (χ') component of ac susceptibility (100~10000 Hz) of 1 at 2500 Oe static field.	20
Figure S25. Argand plots of 1 between 34 K and 50 K from the data at Figure S18 at 2500 Oe static field.	20
Figure S26. Plots of temperature dependent in-phase (χ') and out-of-phase (χ'') components of ac susceptibility (1~1000 Hz) of 1 at 2500 Oe static field.	21
Figure S27. Plots of frequency dependent out-of-phase (χ'') component of ac susceptibility (1~1000 Hz) of 1 at 2500 Oe static field.	21
Figure S28. Plots of frequency dependent in-phase (χ') component of ac susceptibility (1~1000 Hz) of 1 at 2500 Oe static field.	22
Figure S29. Argand plots of 1 between 12 K and 36 K from the data at Figure S22 at 2500 Oe static field.	22
Table S4. Fitting parameters of 1 at 2500 Oe static field.	22
Figure S30. Plots of temperature dependent in-phase (χ') and out-of-phase (χ'') components of ac susceptibility (100~10000 Hz) of 3 under zero static field.	23
Figure S31. Plots of frequency dependent out-of-phase (χ'') component of ac susceptibility (100~10000 Hz) of 3 at zero static field.	24
Figure S32. Plots of frequency dependent in-phase (χ') component of ac susceptibility (100~10000 Hz) of 3 at zero static field.	24
Figure S33. Argand plots of 3 between 33 K and 48 K from the data at Figure S25 at zero static field.	25
Figure S34. Plots of temperature dependent in-phase (χ') and out-of-phase (χ'') components of ac susceptibility (1~1000 Hz) of 3 at zero static field.	25
Figure S35. Plots of frequency dependent out-of-phase (χ'') component of ac susceptibility (1~1000 Hz) of 3 at zero static field.	26
Figure S36. Plots of frequency dependent in-phase (χ') component of ac susceptibility (1~1000 Hz) of 3 at zero static field.	26
Figure S37. Argand plots of 3 between 12 K and 36 K from the data at Figure S29at zero static field.	27

Table S5. Fitting parameters of 3 at zero static field.	27
Figure S38. Plots of temperature dependent in-phase (χ') and out-of-phase (χ'') components of ac susceptibility (100~10000 Hz) of 3 at 2500 Oe static field.	28
Figure S39. Plots of frequency dependent out-of-phase (χ'') component of ac susceptibility (100~10000 Hz) of 3 at 2500 Oe static field.	29
Figure S40. Plots of frequency dependent in-phase (χ') component of ac susceptibility (100~10000 Hz) of 3 at 2500 Oe static field.	29
Figure S41. Argand plots of 3 between 33 K and 48 K from the data at Figure S33at 2500 Oe static field.	30
Figure S42. Plots of temperature dependent in-phase (χ') and out-of-phase (χ'') components of ac susceptibility (1~1000 Hz) of 3 at 2500 Oe static field.	30
Figure S43. Plots of frequency dependent out-of-phase (χ'') component of ac susceptibility (1~1000 Hz) of 3 at 2500 Oe static field.	31
Figure S44. Plots of frequency dependent in-phase (χ') component of ac susceptibility (1~1000 Hz) of 3 at 2500 Oe static field.	31
Figure S45. Argand plots of 3 between 12 K and 36 K from the data at Figure S37at 2500 Oe static field.	32
Table S6. Fitting parameters of 3 at 2500 Oe static field.	32
Table S7. Arrhenius fitting parameters in Figure 5. (ZF=zero field; HF=2500 Oe dc field)	33
Table S8. Dual process fitting parameters in Figure 5. (ZF=zero field; HF=2500 Oe dc field).....	33
IV. Ab initio Calculation	33
Figure S46. The fragment for the <i>ab initio</i> calculation (all H atom are omitted). Arrows show the directions of g_z vectors calculated by the method CAS(11,8) (blue for the ground doublets, red for first-excited doublets and pink for second-excited doublets).....	34
Figure S47. Orientations of the local main magnetizations (blue arrows) of the ground doublets on Dy ^{III} ions of 1	35
Figure S48. Mulliken charges on each atom center of Ln ₂ O ₈ structure in the molecular fragment, blue arrow shows the easy axis of ground doublets.	35
Table S9. Relative energy (E/k_B , K) and effective g values ($S = \pm 1/2$) in xyz direction of the lowest 8 KDs obtained respectively from two kind of <i>ab initio</i> calculations of individual Dy ^{III} fragment.	36
Table S10. <i>Ab initio</i> calculation based composition for the wave functions (wf1 to wf16) corresponding to the 8 Kramers doublets of the ⁶ H _{15/2} multiplet in wave functions with definite projection of the total moment JM>, together with the angle between main axes of corresponding state doublets and the ground state doublets.....	36
V. Magnetic interaction analysis	37
Table S11. Calculated energies (cm ⁻¹), the corresponding tunneling gaps (cm ⁻¹) and the g_z values of the low-lying exchange doublet states of complex 1	38
Figure S49. A comparison of the experimental (black dots) and calculated (red solid line) magnetic susceptibility using POLY_ANISO for complex 1	38
Figure S50. A comparison of the experimental (black dots) and calculated (line) magnetic susceptibility for complex 4 . The red and green line were obtained using numerical method, the blue line was obtained using van Vleck equation.	39
Reference	39

I. Synthetic procedures

The present compounds are all air sensitive. Therefore, all manipulations were carried out using glove box techniques under an atmosphere of dry argon, if without special descriptions. The vapour diffusion reactions were carried out in an h-type tube sealed *in vacuo* near 77 K. All solvents were treated under solution treatment system (BRAUN MB-SPS800). Rare Earth salts were purchased from Boron Chemicals. KN^* ($\text{N}^* = [\text{N}(\text{SiMe}_3)_2]^-$) was purified after received (Sigma-Aldrich). H-DBP (Sigma-Aldrich) and NaN^* (Alfa Aesar) were used as received. The ICP-AES was performed using Leeman PROFILE SPEC spectrometer. Elementar Analysensysteme GmbH vario EL was used as elemental analyzer.

The synthetic route of complex **1-3** is shown in Scheme S1.



Scheme S1. The synthesis method of complex **1-4**.

Purification of KN^* : KN^* (95%) received from Sigma-Aldrich was dissolved in excess toluene. Stirred overnight, centrifuged to remove the insoluble oil-like substances, colorless solution was obtained. Removing solvents *in vacuo*, white powders was collected for future reactions.

Synthesis of DyN_3^* : The synthesis of DyN_3^* was followed by the reported works¹ but with small modification. The reactant LiN^* was replaced by KN^* . The reaction of DyCl_3 (1.0754 g, 4 mmol) with KN^* (2.3938 g, 12 mmol) in 40 ml THF gave very pale yellow powder 1.2321 g. (Yield 48% in Y, not optimized)

Synthesis of YN_3^* : Following the procedure described for DyN_3^* . The reaction of YCl_3 (0.7810 g, 4 mmol) with KN^* (2.3938 g, 12 mmol) gave white powder 1.0708 g. (Yield 47% in Y, not optimized)

Synthesis of GdN_3^* : Following the procedure described for DyN_3^* . The reactant KN^* was replaced by NaN^* . The reaction of GdCl_3 (1.0894 g, 4 mmol) with KN^* (2.2737 g, 12 mmol) gave white powder 1.5885 g. (Yield 62% in Gd, not optimized)

Synthesis of $[\text{Dy}(\mu\text{-OH})(\text{DBP})_2(\text{THF})]_2(\mathbf{1})$: DyN_3^* (0.1290 g, 0.2 mmol) was dissolved in hexane(2 ml), and then mixed with a solution of H-DBP(0.1654 g, 0.8 mmol) in toluene(2 ml). After a vapor diffusion with H_2O (3.6 μl , 0.2 mmol) in 2 ml THF (less than 2 days), clear light greenish yellow crystals (0.0726 g) were obtained. (Yield 27% in Dy, not optimized. Elemental analysis for $\text{C}_{64}\text{H}_{102}\text{O}_8\text{Dy}_2$: Calcd 58.04 % C, 7.76% H, 0% N. Found 58.26% C, 7.72% H, 0.00% N.)

Synthesis of $[\text{Y}(\mu\text{-OH})(\text{DBP})_2(\text{THF})]_2(\mathbf{2})$: YN_3^* (0.0567 g, 0.1 mmol) was dissolved in hexane(2 ml), and then mixed with a solution of H-DBP(0.0825 g, 0.4 mmol) in toluene(2 ml). After a gas diffusion with H_2O (1.8 μl , 0.1 mmol) in THF (2 ml), clear colourless crystals (0.0308 g) were obtained. (Yield 13% in Y, not optimized. Elemental analysis for $\text{C}_{64}\text{H}_{102}\text{O}_8\text{Y}_2$: Calcd 65.29% C, 8.73% H, 0% N. Found 65.56% C, 8.54% H, 0.00% N.)

Synthesis of Dy@[Y(μ -OH)(DBP)₂(THF)]₂(**3**): Following the procedure described for Complex **1**. The reactants were changed to DyN₃⁺ (0.0129 g, 0.02 mmol), YN₃⁺ (0.2167 g, 0.38 mmol), H-DBP (0.3299 g, 1.6 mmol) and H₂O (7.2 μ l, 0.4 mmol). The vapor diffusion gave clear light yellow crystals 0.1477 g. (Yield 31% in Ln, not optimized. Elemental analysis for C₆₄H₁₀₂O₈Y_{1.9}Dy_{0.1}: Calcd 64.89% C, 8.68% H, 0% N. Found 65.10% C, 8.58% H, 0.00% N. ICP-AES was used to determine the molar ratio Dy:(Dy+Y) = 5%.) The synthesis have been repeated for several times. The molar ratios Dy:(Dy+Y) were in the ranged of 3%-6%, and the elemental analysis correspondingly matched within the apparatus error (\pm 0.3%).

Synthesis of [Gd(μ -OH)(DBP)₂(THF)]₂(**4**): GdN₃⁺ (0.1274 g, 0.2 mmol) was dissolved in hexane (2 ml), and then mixed with a solution of H-DBP (0.1654 g, 0.8 mmol) in toluene (2 ml). After a gas diffusion with H₂O (1.8 μ l, 0.1 mmol) in THF (2 ml), clear colourless crystals (0.0818 g) were obtained. (Yield 31% in Gd, not optimized. Elemental analysis for C₆₄H₁₀₂O₈Gd₂: Calcd 58.50% C, 7.82% H, 0% N. Found 58.47% C, 7.69% H, 0.00% N.)

II. Structure

Method

Single-crystal XRD data were collected at the temperature of 180 K on an *Agilent technologies Super Nova Atlas Dual System* with an alternative microfocus source (Mo K α = 0.710 73 Å, Cu K α = 1.54184 Å) and focusing multilayer mirror optics. Suitable crystals (with dimensions of 0.42 \times 0.36 \times 0.22 mm³ for compound **1**, 0.11 \times 0.08 \times 0.08 mm³ for compound **2** and 0.16 \times 0.12 \times 0.09 mm³ for compound **4**) were mounted under nitrogen atmosphere, and the data was collected with Mo K α microfocus source. The data processing was accomplished with the *CrysAlisPro* program. The structures were solved by direct methods and refined on F^2 anisotropically for all the non-hydrogen atoms by the full-matrix least-squares method using *SHELXL 97* program². Details data were listed in Table S1.

High resolution powder XRD experiments were performed on a *PAN analytical X'Pert PRO* diffractometer equipped with a Pixel detector and using Cu K α source (1.5406 Å). The crystals of compound **1-3** were crushed to powder and sealed in 0.5 mm diameter glass capillaries. During the experiment, the capillaries were spun continuously. The data were collected under ambient temperature. *Mercury 3.8* program was used to simulate the reference patterns based on the crystal structures obtained with single-crystal XRD.

FT-IR spectra were collected at ambient temperature and pressure using *Bruker Tensor 27* spectrometer. The crystals of compound **1-4** and Dy(DBP)₃ (for comparison) were crushed to powder and sandwiched between two KBr crystal tablets of 50 \times 50 \times 30 mm³. Parafilm was twined along the side for temporary sealing to protect from air during experiments. Baseline and smooth correction were performed on the raw spectroscopies.

Results and discussion

As Table 1 shown, the slight difference between **1** and **3** is the relative length of the two Ln-OH bonds. *SHAPE 2.0* program was used to generate CShM's values to search the possible geometric symmetry of the first coordination sphere.³ CShM's value is a kind of index to evaluate geometric similarity of coordination polyhedrons. Smaller CShM's means that two polyhedrons are closer, and zero value means two polyhedrons are geometrically identical. The first coordination sphere was compared with all reference polyhedrons with five vertices. As Table S2 shown, the smallest CShM's value of all is larger than 1.8, indicating large deviation from standard polyhedrons.

PXRD patterns (Figure S1) indicate the diluted compound **3** is pure single-phase, which is isostructural to **2**. This is coincided with the results of dc magnetism.

FT-IR spectrum (Figure S2) of a three-coordinate Dysprosium compound with the same phenolate ligands, Dy(DBP)₃, was also collected for comparison since it contains no O-H bonds. Sharp absorption peaks around 3670 cm⁻¹ were detected for all hydroxide-bridged dimers (compound **1-4**), but not observed for Dy(DBP)₃. These are the fingerprint peaks of O-H stretching without H-bonding acceptors. The other peaks larger than 500 cm⁻¹ were almost the same for these five samples. The different peaks below 500 cm⁻¹ may be the consequence of different Ln-O bonds, or the transition between low lying states.

Table S1. Crystallographic data and structure refinements of Compound **1**, **2** and **4**.

<i>Compound</i>	1	2	4
Formula	C ₆₄ H ₁₀₂ Dy ₂ O ₈	C ₆₄ H ₁₀₂ Y ₂ O ₈	C ₆₄ H ₁₀₂ Gd ₂ O ₈
Formula weight	1324.46	1177.28	1313.96
Crystal system	Orthorhombic	Orthorhombic	Orthorhombic
Space-group	<i>P b c a</i>	<i>P b c a</i>	<i>P b c a</i>
<i>a</i> , Å	19.3566(3)	19.3525(5)	19.3419(3)
<i>b</i> , Å	15.6297(2)	15.6285(3)	15.6815(1)
<i>c</i> , Å	20.7260(3)	20.6896(5)	20.7720(3)
<i>V</i> , Å ³	6270.38(18)	6275.6(2)	6300.37(14)
<i>Z</i>	4	4	4
<i>T</i> , K	180	180	180
F(000)	2728.0	2512.0	2712.0
λ , Å	0.71073	0.71073	0.71073
Data completeness	0.999	1.000	0.999
R1	2.52%	3.73%	2.37%
wR2 (all data)	6.16%	8.31%	5.35%
S	1.142	1.026	1.138
Bond precision (C-C), Å	0.0040	0.0031	0.0037

Table S2. The CShM's values of the first coordination sphere of compound **1** and **2**, referring to all standard 5 vertices polyhedrons.

REFERENCE SHAPES	PENTAGON	VOCANT OCTAHEDRON	TRIGONAL BIPYRAMID	SQUARE PYRAMID	JOHNSON TRIGONAL BIPYRAMID
------------------	----------	-------------------	--------------------	----------------	----------------------------

SYMMETRY	D _{5h}	C _{4v}	D _{3h}	C _{4v}	D _{3h}
COMPOUND 1	30.530	4.354	2.756	1.923	6.089
COMPOUND 2	30.328	4.274	2.850	1.825	6.101

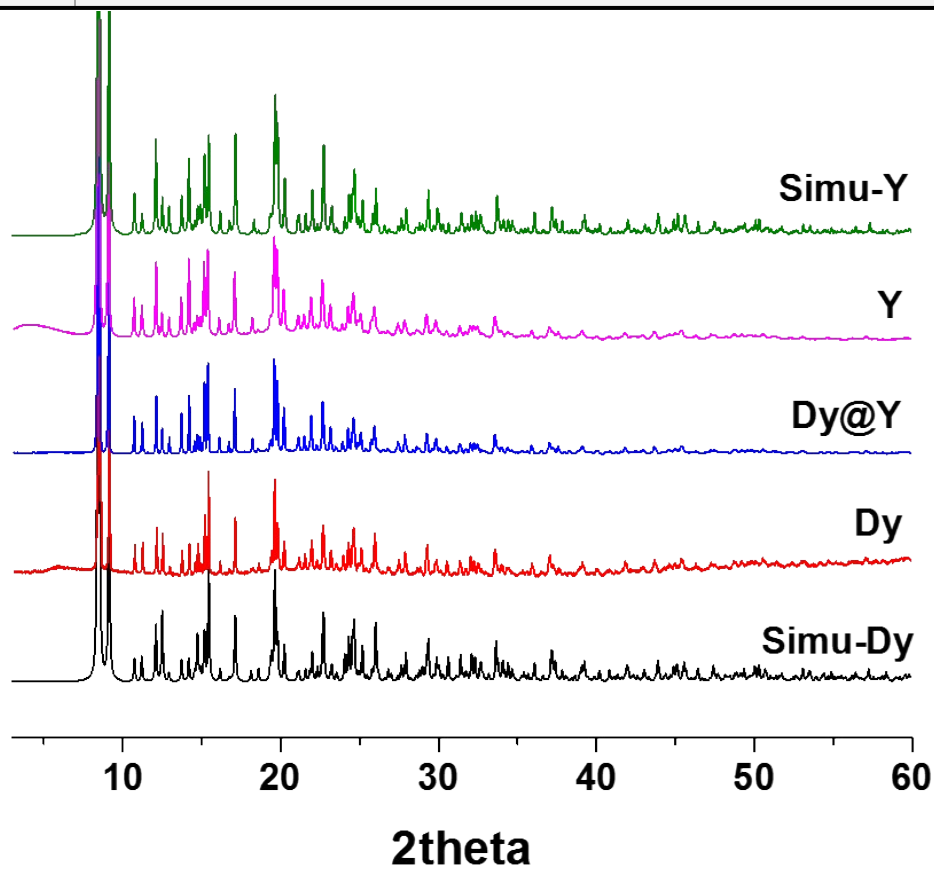


Figure S1. Powder XRD patterns of compound 1-3 and simulated patterns of 1 and 2.

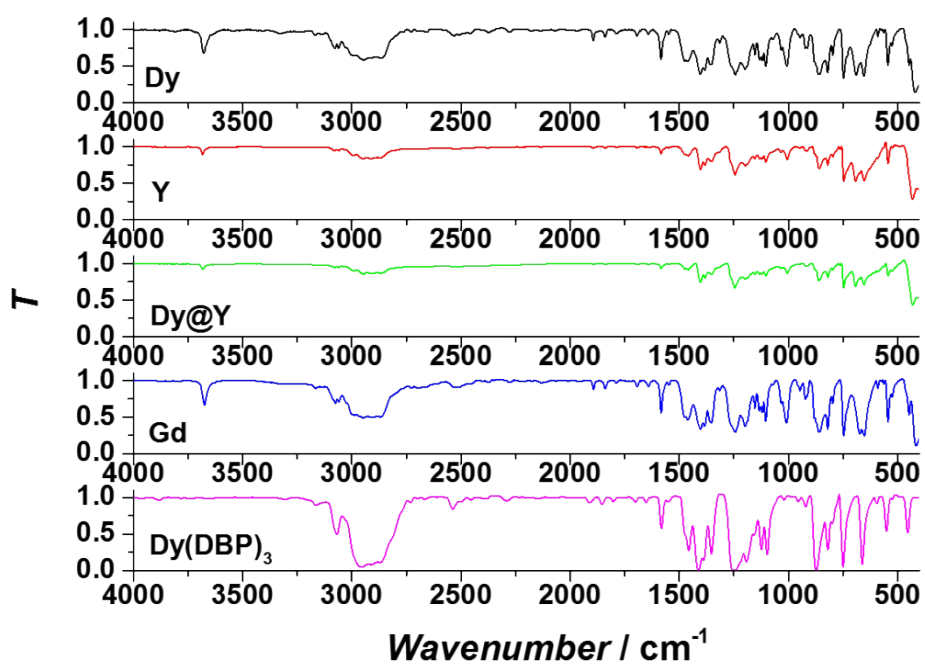


Figure S2. FT-IR spectra of compound 1-4 and $\text{Dy}(\text{DBP})_3$ at the range of 400~4000 cm^{-1} .

III. Magnetism

Method

The samples were stuffed in capsules with parafilm covered to protect them from air and water. Ac magnetic measurement data of poly crystals were collected both on Quantum Design PPMS magnetometer (100~10000 Hz) and Quantum Design MPMS XL-5 SQUID magnetometer (1~1000 Hz). Dc magnetism except the hysteresis of poly crystals were performed on Quantum Design MPMS XL-5 SQUID magnetometer (RSO/DC module). The hysteresis measurements were performed on Quantum Design MPMS3 magnetometer (VSM module). Capsule, parafilm and molecule formula (Pascal constant) were considered when the diamagnetic correction was carried on the data.

Results and discussion

As Figure S13, S22 and S26 shown, both in phase (χ_m') and out-of-phase (χ_m'') ac susceptibilities retained almost the same when the dc field was smaller than 1750 Oe. After that, the signals began to increase. Peaks were observed at 2500 Oe. This behavior coincides with the intramolecular antiferromagnetic Dy^{III}-Dy^{III} interaction. On one hand, as the results of hysteresis measurements, when the applied dc field is near 2500 Oe, a level-crossing process occurred. Resonance with level-crossing process raise up the χ_m'' . On the other hand, the level-crossing process of the two Dy^{III} lead to less population of the antiferromagnetic coupling ground state, hence the susceptibility raised up, which also made contributions to the raise of both χ_m' and χ_m'' components.

Cole-Cole fitting was done to obtain the χ_t , χ_s and α , then fitting $\chi_m''-f$ curves with obtained χ_t , χ_s and α as constants gave the corresponding relaxation time, τ . The fitting models of relaxation process does not include QTM process since its contribution could be omitted in the fitting regime. In addition, the process is slower than 1 Hz (Figure S18 and S34), which is out of our range of measurement, hence the accurate τ_{QTM} could not be obtained directly by our measurements.

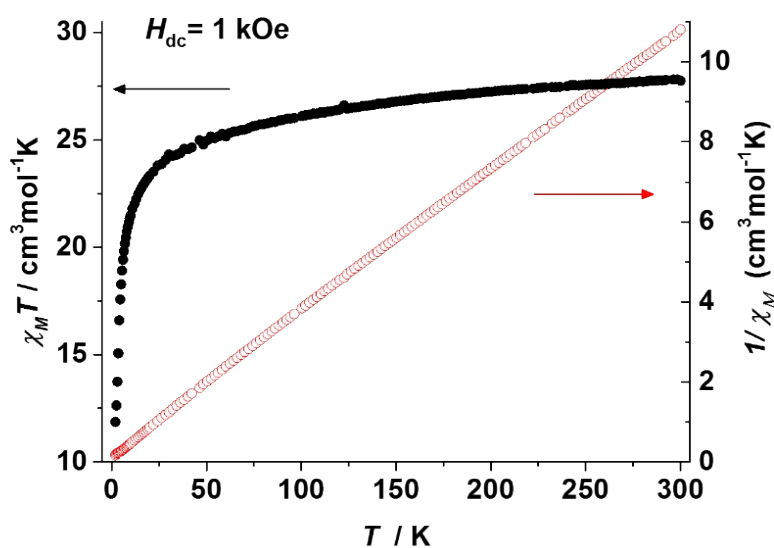


Figure S3. Temperature dependence of $\chi_M T$ and χ_M^{-1} for a polycrystalline sample of 1.

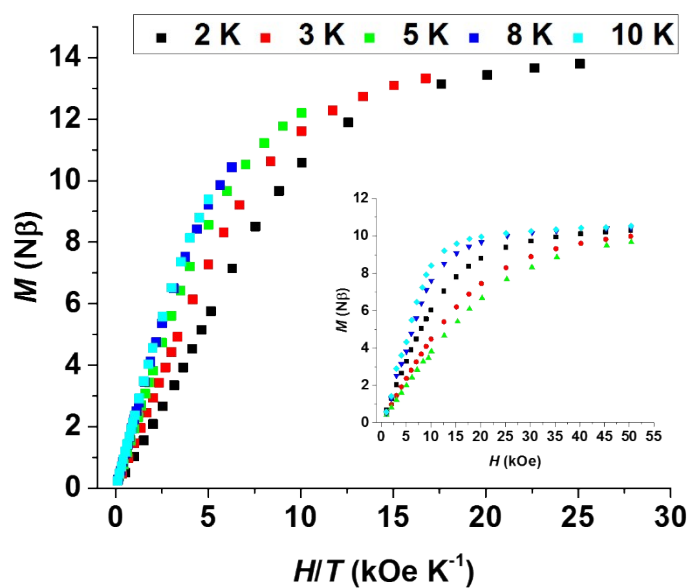


Figure S4. Plots of the reduced magnetization M vs H/T at the temperatures of 2 K, 3 K, 5 K, 8 K and 10 K for a polycrystalline sample of **1**.

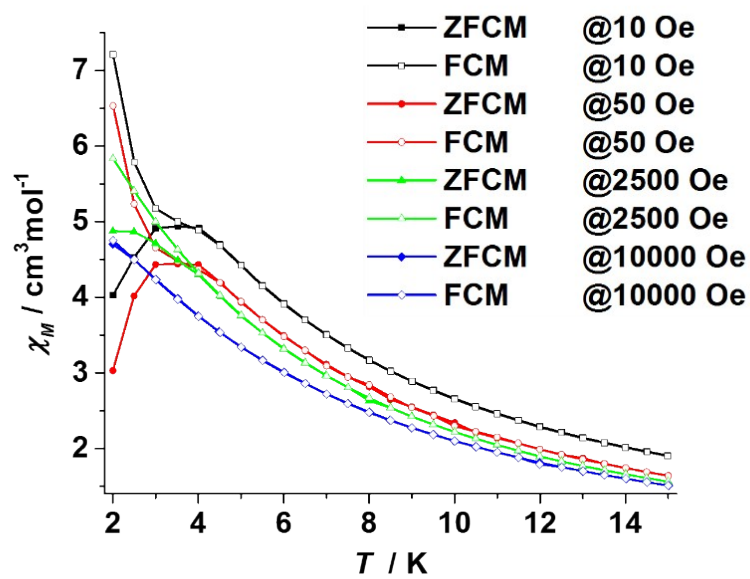


Figure S5. Plots of zero-field-cooled magnetization (ZFCM) and field-cooled magnetization (FCM) for a polycrystalline sample of **1** under 10 Oe, 50 Oe, 2500 Oe and 10000 Oe.

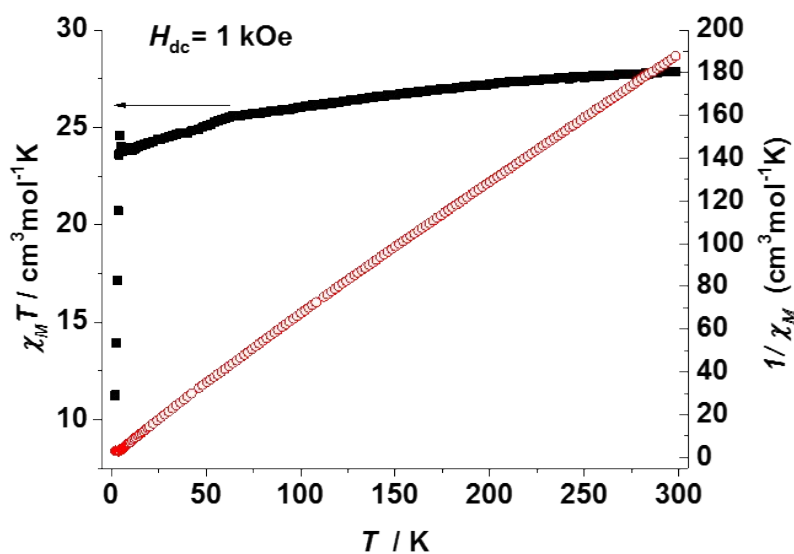


Figure S6. Temperature dependence of $\chi_M T$ and χ_M^{-1} for a polycrystalline sample of **3**. (χ_M was divided by the Dy ratio.)

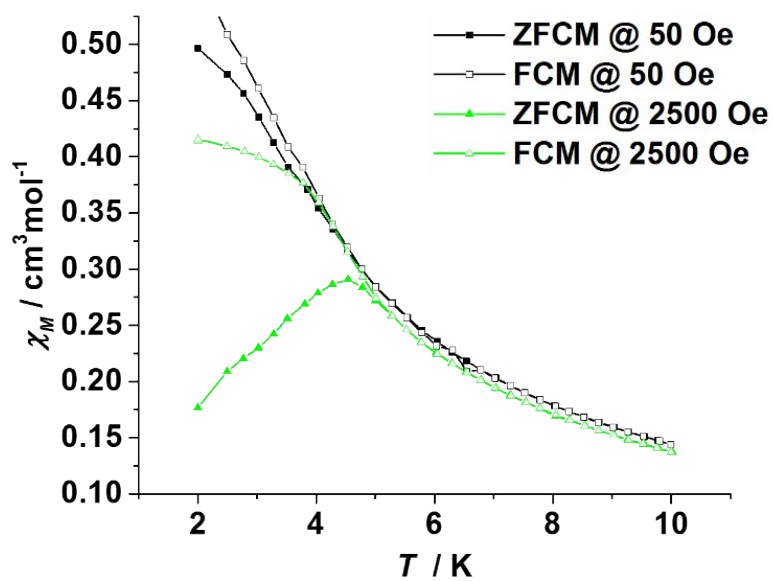


Figure S7. Plots of zero-field-cooled magnetization (ZFCM) and field-cooled magnetization (FCM) for a polycrystalline sample of **3** under 50 Oe and 2500 Oe.

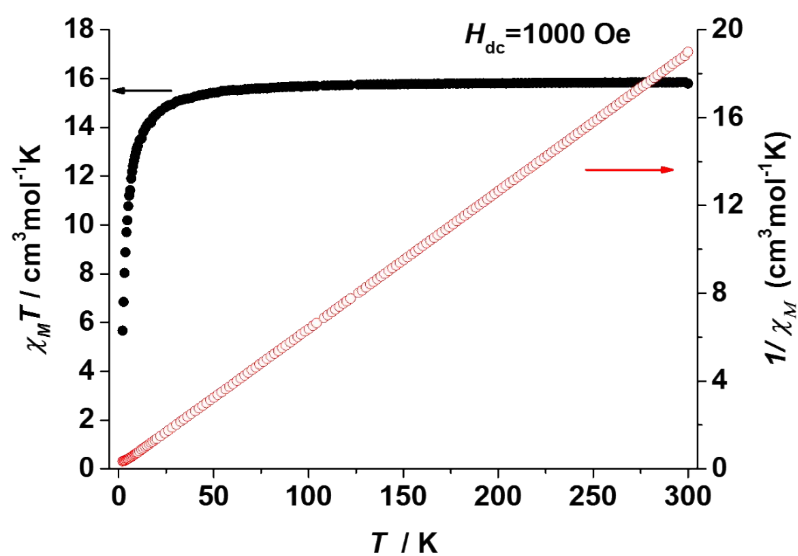


Figure S8. Temperature dependence of $\chi_M T$ and χ_M^{-1} for a polycrystalline sample of **4**.

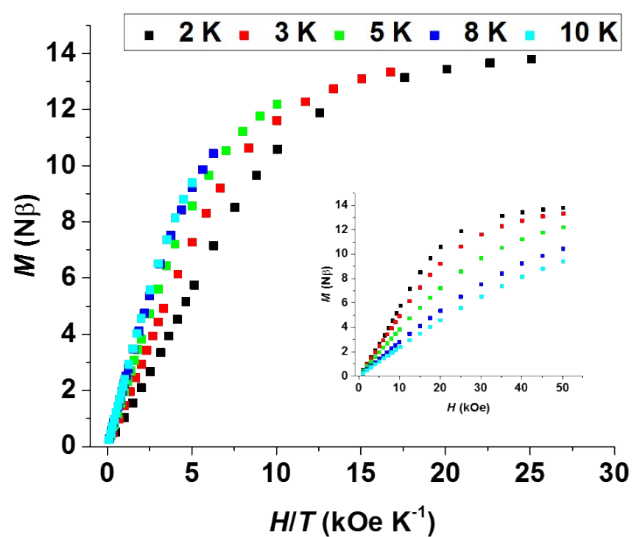


Figure S9. Plots of the reduced magnetization M vs H/T at the temperatures of 2 K, 3 K, 5 K, 8 K and 10 K for a polycrystalline sample of **4**. Insert: plots of M vs H .

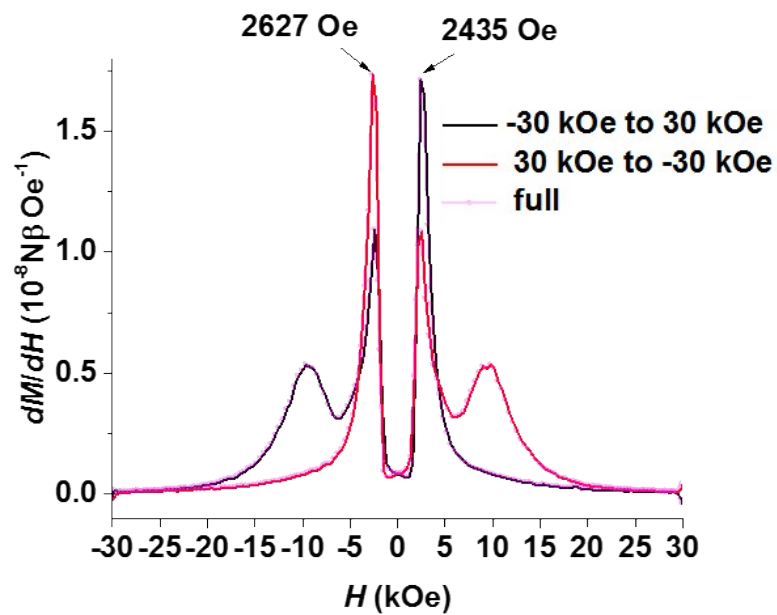


Figure S10. The first derivative of magnetization (dM/dH) of complex 1 versus magnetic field for the curves measured at 2 K at scan rate of 200 Oe/s, sweep mode.

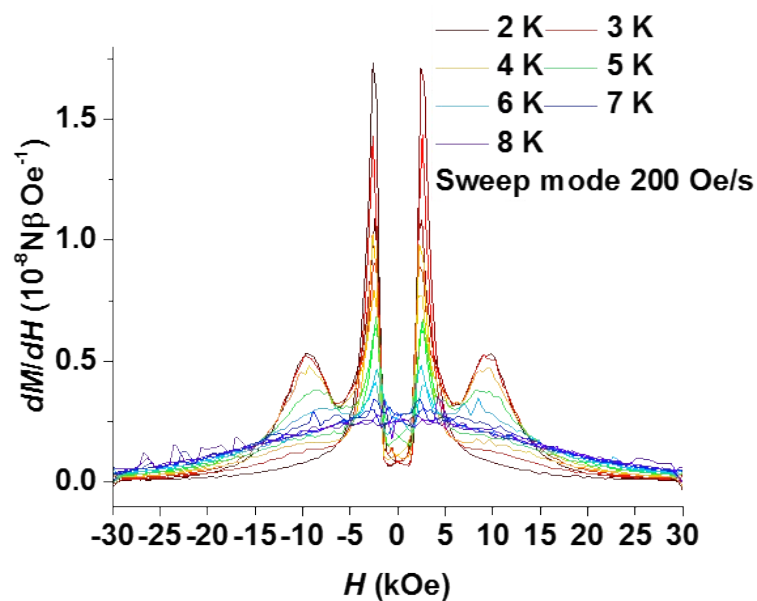


Figure S11. The first derivative of magnetization (dM/dH) of complex 1 versus magnetic field for the curves measured at different temperature at scan rate of 200 Oe/s, sweep mode.

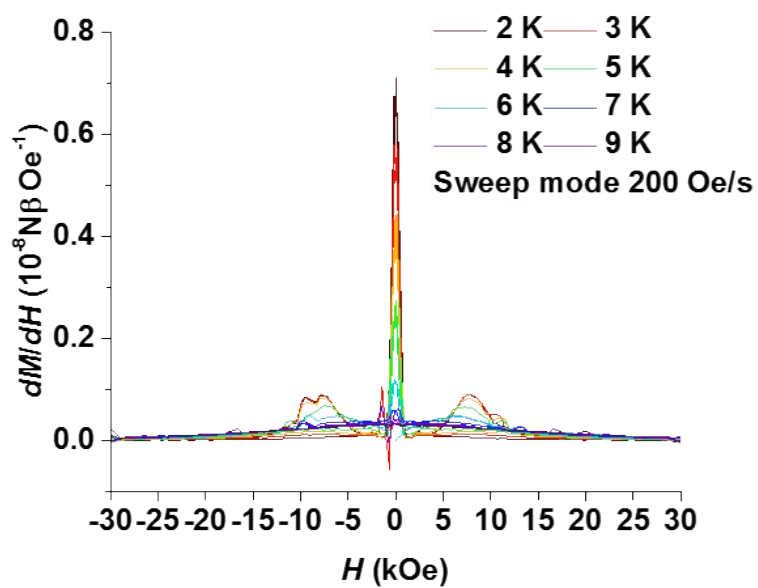


Figure S12. The first derivative of magnetization (dM/dH) of complex **3** versus magnetic field for the curves measured at different temperature at scan rate of 200 Oe/s, sweep mode.

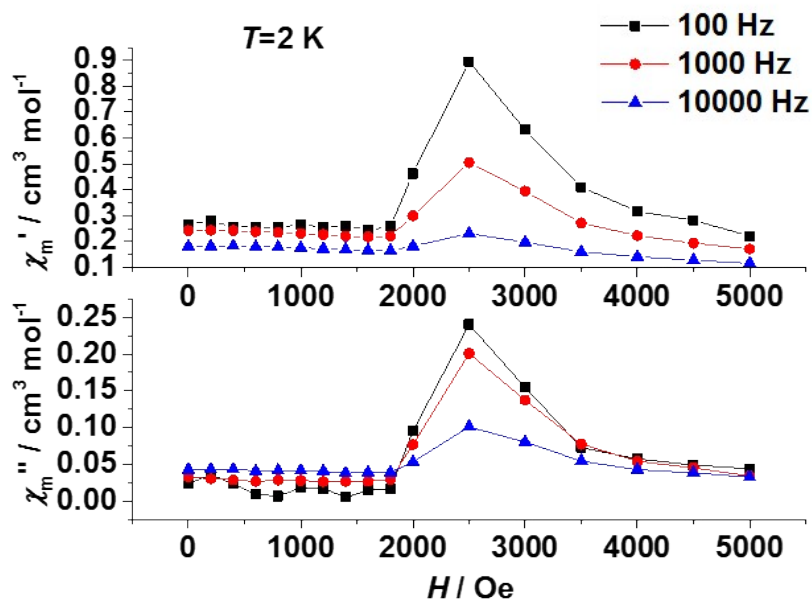


Figure S13. Plots of magnetic field dependent in-phase (χ') and out-of-phase (χ'') components of ac susceptibility (100~10000 Hz) of **1** at 2 K.

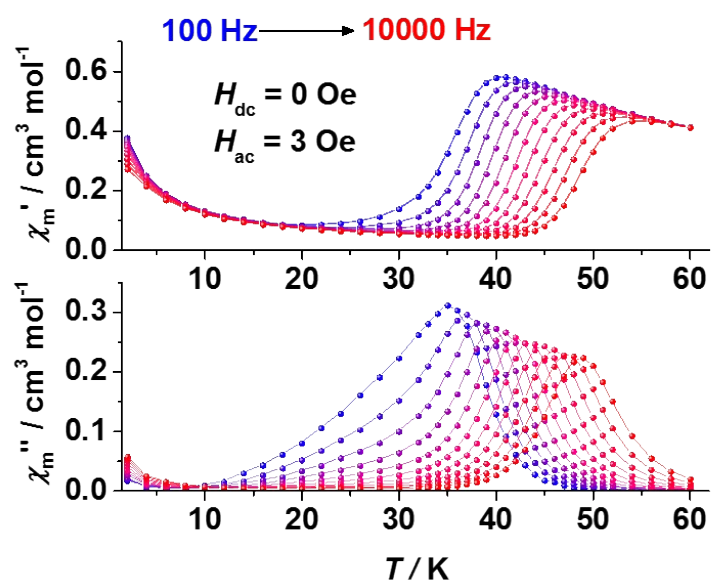


Figure S14. Plots of temperature dependent in-phase (χ') and out-of-phase (χ'') components of ac susceptibility (100~10000 Hz) of **1** under zero static field.

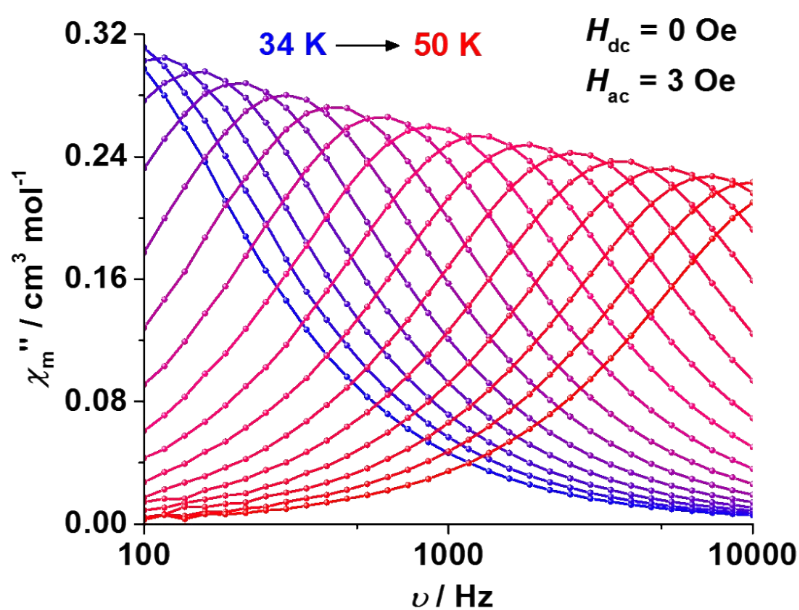


Figure S15. Plots of frequency dependent out-of-phase (χ'') component of ac susceptibility (100~10000 Hz) of **1** at zero static field.

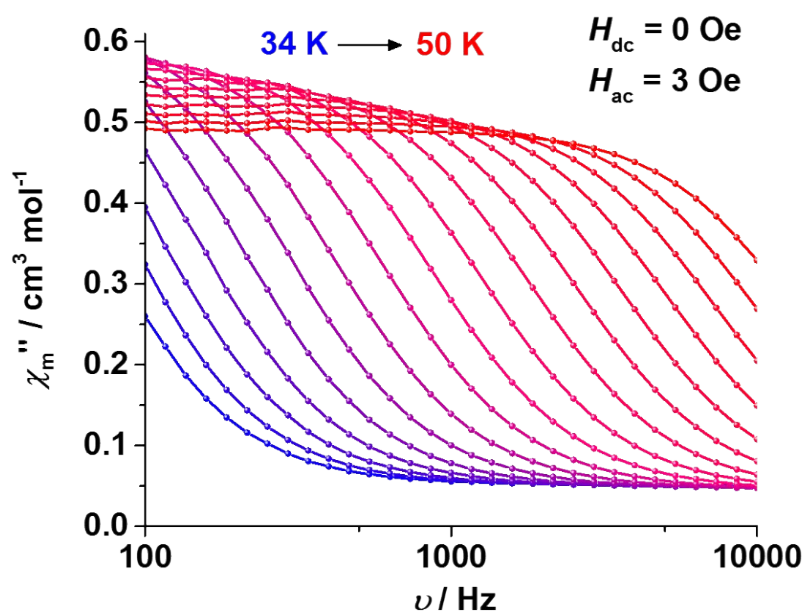


Figure S16. Plots of frequency dependent in-phase (χ') component of ac susceptibility (100~10000 Hz) of **1** at zero static field.

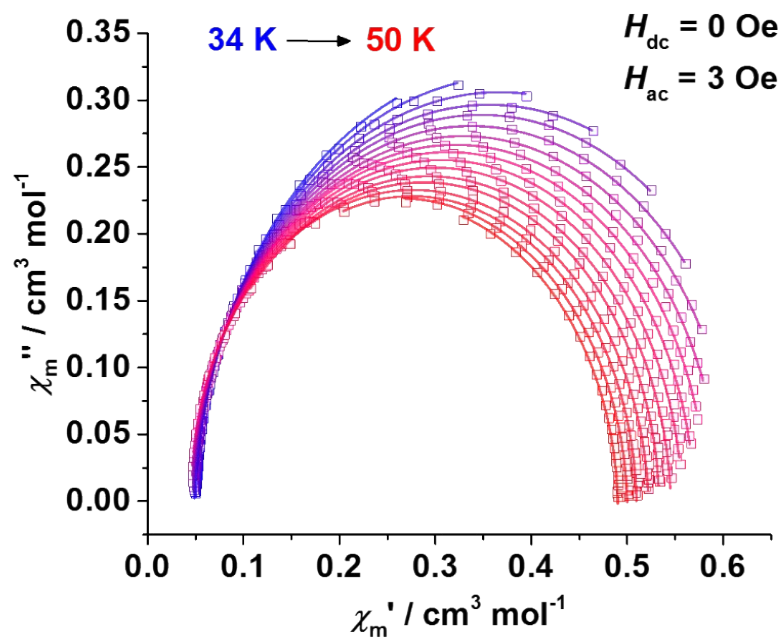


Figure S17. Argand plots of **1** between 34 K and 50 K from the data at Figure S10 at zero static field. .

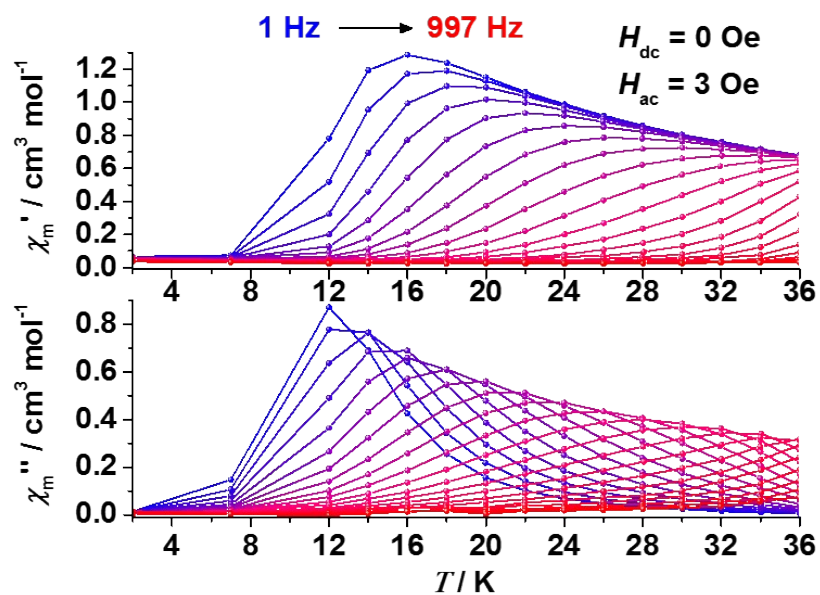


Figure S18. Plots of temperature dependent in-phase (χ') and out-of-phase (χ'') components of ac susceptibility (1~1000 Hz) of 1 at zero static field.

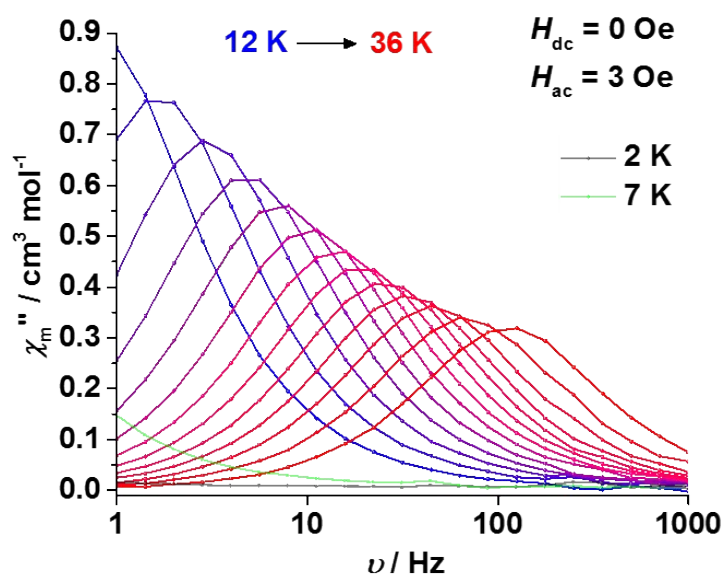


Figure S19. Plots of frequency dependent out-of-phase (χ'') component of ac susceptibility (1~1000 Hz) of 1 at zero static field.

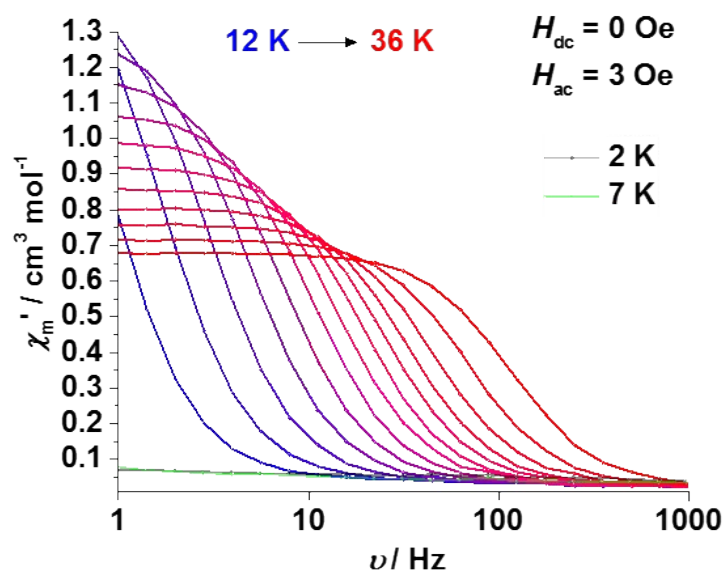


Figure S20. Plots of frequency dependent in-phase (χ') component of ac susceptibility (1~1000 Hz) of **1** at zero static field.

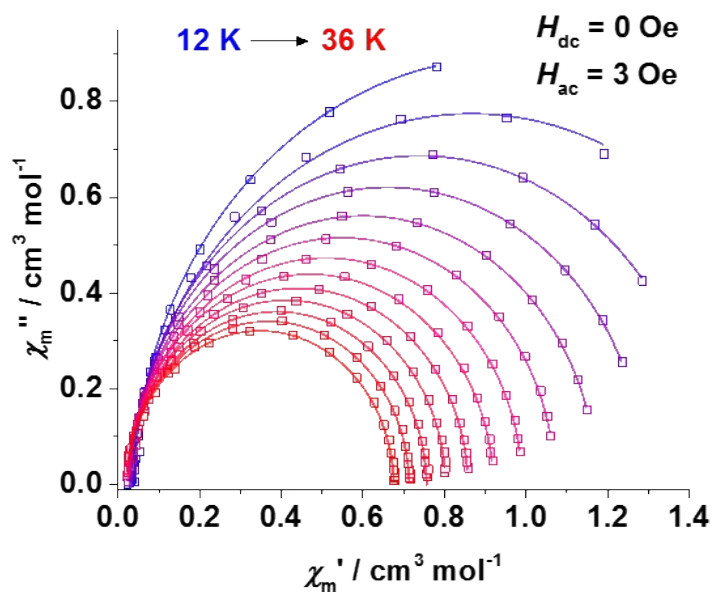


Figure S21. Argand plots of **1** between 12 K and 36 K from the data at Figure S14 at zero static field.

Table S3. Fitting parameters of **1** at zero static field.

Data corrected on MPMS (1~1000 Hz)				
Temperature (K)	χ_t (emu mol ⁻¹)	χ_s (emu mol ⁻¹)	α	τ (s)
12	0.04013	1.88525	0.0224	1.967E-01
14	0.0303	1.70807	0.05223	1.016E-01
16	0.03311	1.45058	0.02204	5.405E-02

18	0.03192	1.29705	0.01421	3.329E-02
20	0.02968	1.1781	0.01732	2.208E-02
22	0.02993	1.07482	0.01162	1.539E-02
24	0.02881	0.99408	0.01576	1.117E-02
26	0.02271	0.92315	0.01937	8.320E-03
28	0.02663	0.86063	0.01514	6.270E-03
30	0.02437	0.8055	0.01347	4.740E-03
32	0.02603	0.75905	0.01445	3.460E-03
34	0.02417	0.71653	0.0152	2.320E-03
36	0.02251	0.67896	0.01955	1.400E-03
Data corrected on PPMS (100~10000 Hz)				
Temperature (K)	χ_r (emu mo l⁻¹)	χ_s (emu mol⁻¹)	α	τ (s)
34	0.05048	0.74086	0.03143	2.52E-3
35	0.04951	0.71616	0.03079	1.97E-3
36	0.04864	0.68763	0.02864	1.47E-3
37	0.04777	0.66699	0.02855	1.08E-3
38	0.0469	0.65118	0.02954	7.81474E-4
39	0.04606	0.63182	0.02837	5.47741E-4
40	0.04522	0.61516	0.02842	3.80728E-4
41	0.04458	0.59947	0.02671	2.63757E-4
42	0.04437	0.58467	0.02302	1.82087E-4
43	0.04389	0.57156	0.02271	1.26211E-4
44	0.04362	0.55873	0.0219	8.7853E-5
45	0.04174	0.54699	0.02619	6.13252E-5
46	0.04304	0.5348	0.02101	4.34715E-5
47	0.0334	0.52377	0.03472	3.03701E-5
48	0.04217	0.51102	0.01896	2.22919E-5
49	0.02925	0.50143	0.02829	1.55853E-5
50	0.0258	0.4916	0.02669	1.12759E-5

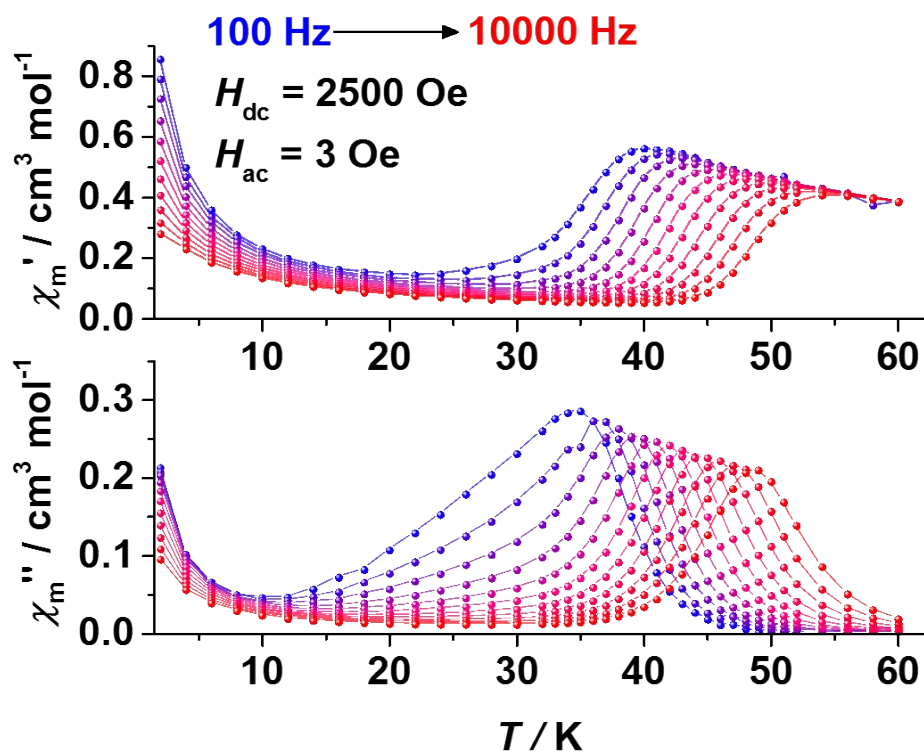


Figure S22. Plots of temperature dependent in-phase (χ') and out-of-phase (χ'') components of ac susceptibility (100~10000 Hz) of **1** at 2500 Oe static field.

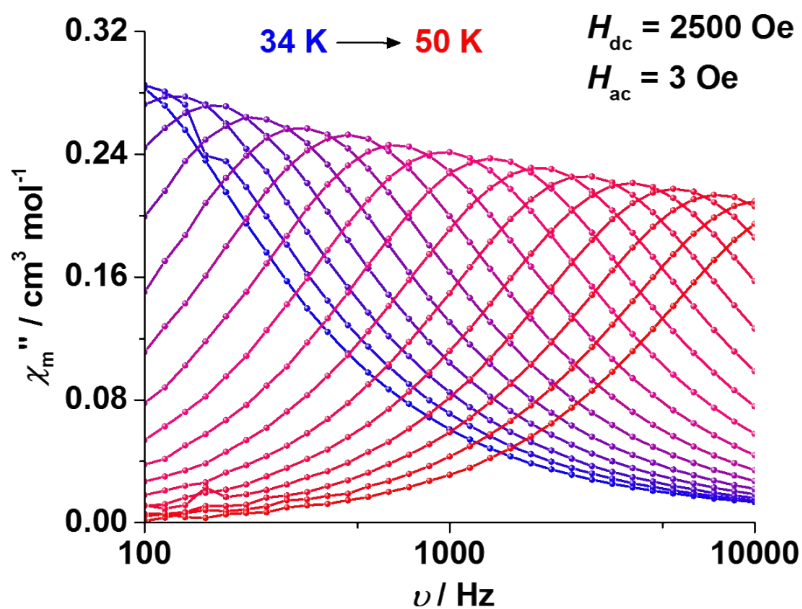


Figure S23. Plots of frequency dependent out-of-phase (χ'') component of ac susceptibility (100~10000 Hz) of **1** at 2500 Oe static field.

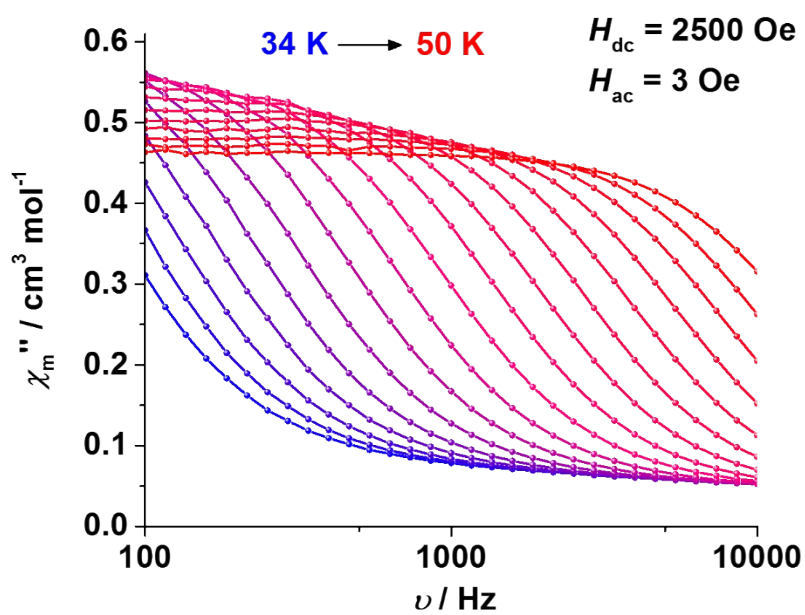


Figure S24. Plots of frequency dependent in-phase (χ'') component of ac susceptibility (100~10000 Hz) of **1** at 2500 Oe static field.

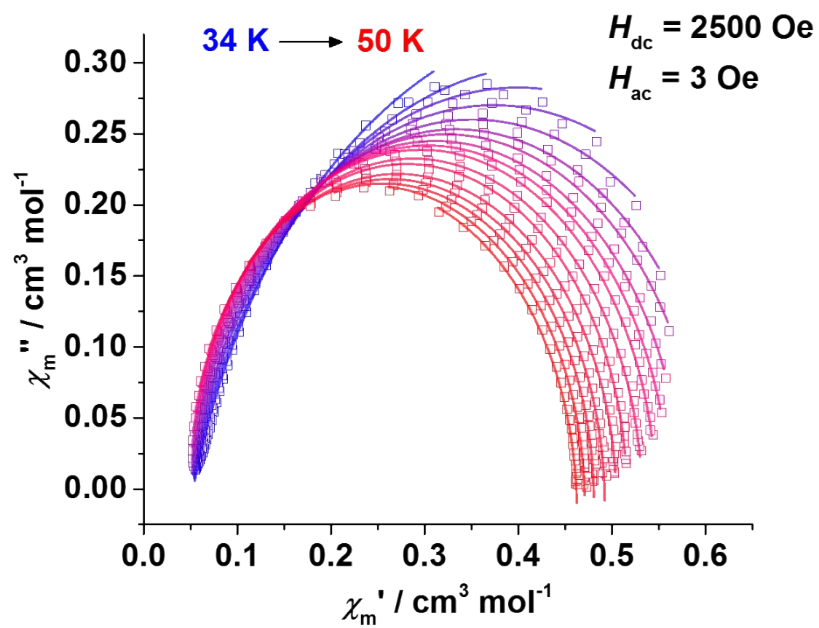


Figure S25. Argand plots of **1** between 34 K and 50 K from the data at Figure S18 at 2500 Oe static field. .

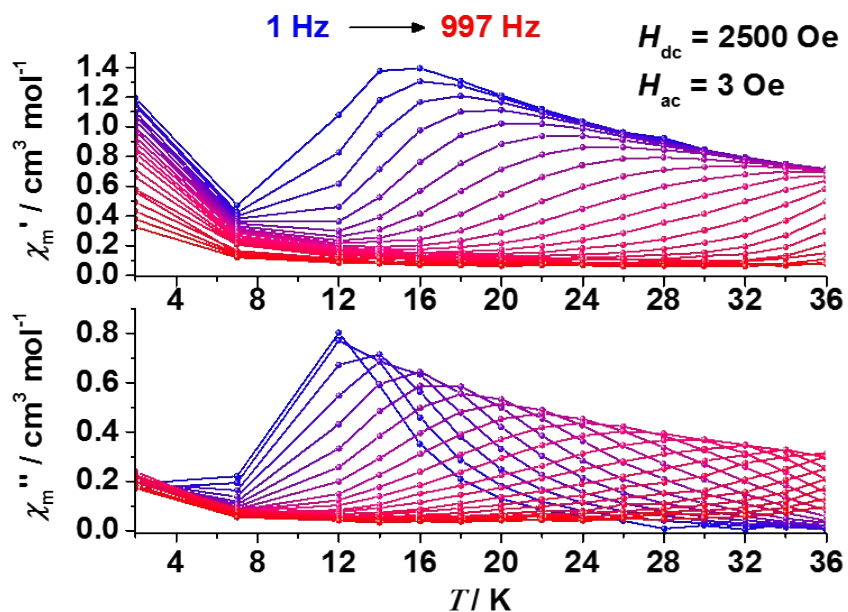


Figure S26. Plots of temperature dependent in-phase (χ') and out-of-phase (χ'') components of ac susceptibility (1~1000 Hz) of **1** at 2500 Oe static field.

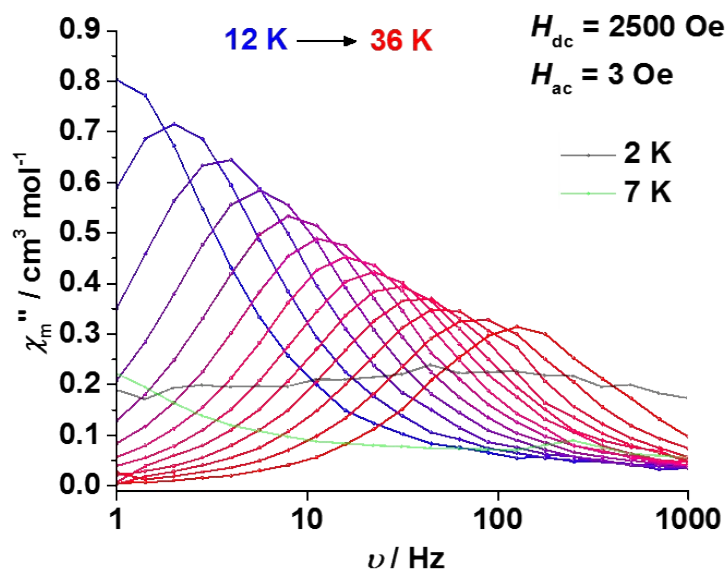


Figure S27. Plots of frequency dependent out-of-phase (χ'') component of ac susceptibility (1~1000 Hz) of **1** at 2500 Oe static field.

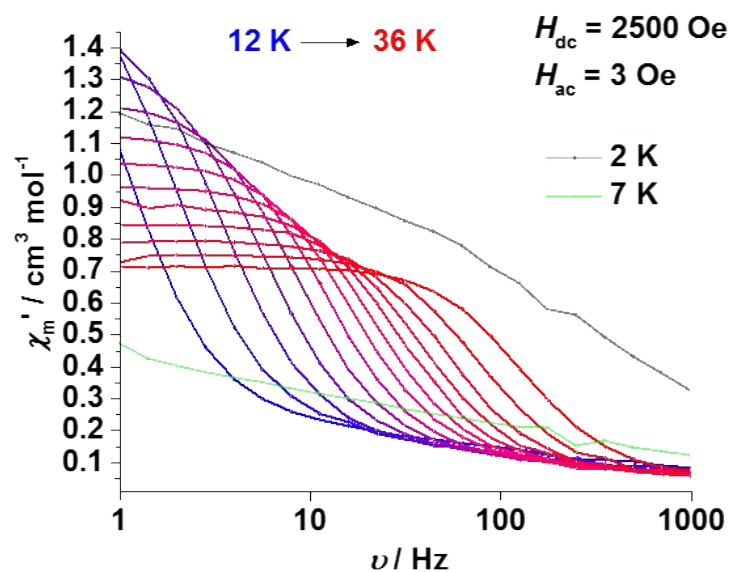


Figure S28. Plots of frequency dependent in-phase (χ') component of ac susceptibility (1~1000 Hz) of **1** at 2500 Oe static field.

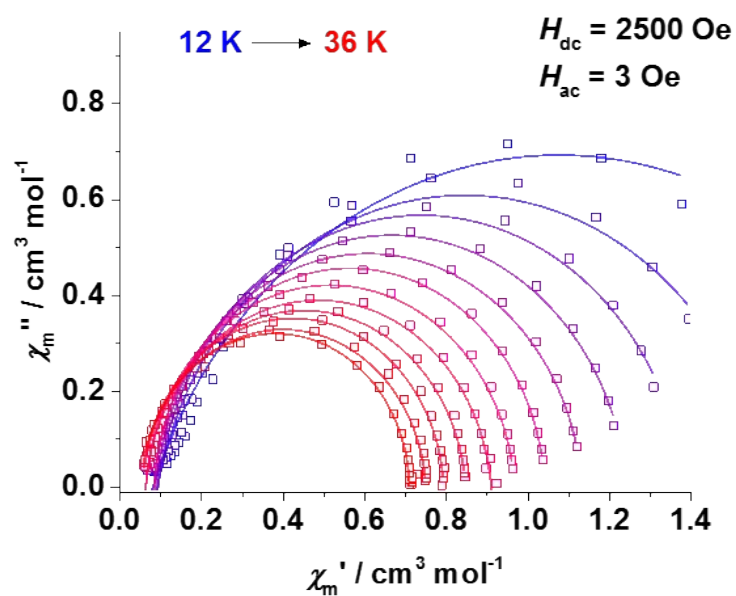


Figure S29. Argand plots of **1** between 12 K and 36 K from the data at Figure S22 at 2500 Oe static field.

Table S4. Fitting parameters of **1** at 2500 Oe static field.

Data corrected on MPMS (1~1000 Hz)				
Temperature (K)	χ_t (emu mol ⁻¹)	χ_s (emu mol ⁻¹)	α	τ (s)
14	0.08362	2.07542	0.22781	1.066E-01
16	0.0949	1.60068	0.13615	4.551E-02
18	0.09557	1.38853	0.08542	2.716E-02

20	0.09119	1.24575	0.06234	1.799E-02
22	0.08489	1.13586	0.05107	1.260E-02
24	0.0871	1.04448	0.03318	9.160E-03
26	0.06584	0.97043	0.04874	6.800E-03
28	0.06497	0.91206	0.05644	5.190E-03
30	0.05677	0.84985	0.05112	3.970E-03
32	0.05435	0.79615	0.03729	2.880E-03
34	0.05166	0.75254	0.04521	1.970E-03
36	0.05584	0.71224	0.02057	1.220E-03
Data corrected on PPMS (100~10000 Hz)				
Temperature (K)	χ_t (emu mo l⁻¹)	χ_s (emu mol⁻¹)	α	τ (s)
35	0.05294	0.81572	0.15594	2.27E-3
36	0.05195	0.75066	0.13502	1.55E-3
37	0.05091	0.69962	0.11677	1.06E-3
38	0.04977	0.65538	0.09754	7.13367E-4
39	0.04905	0.6214	0.07902	4.85659E-4
40	0.04794	0.601	0.06616	3.37067E-4
41	0.04726	0.57809	0.05222	2.33271E-4
42	0.04653	0.56335	0.04385	1.61923E-4
43	0.04635	0.54886	0.03386	1.13412E-4
44	0.04453	0.53369	0.0337	7.9721E-5
45	0.04661	0.51751	0.01995	5.68689E-5
46	0.03866	0.50604	0.03486	4.00423E-5
47	0.0355	0.49349	0.03272	2.87434E-5
48	0.03304	0.482	0.02901	2.07028E-5
49	0.02278	0.47213	0.03518	1.46165E-5

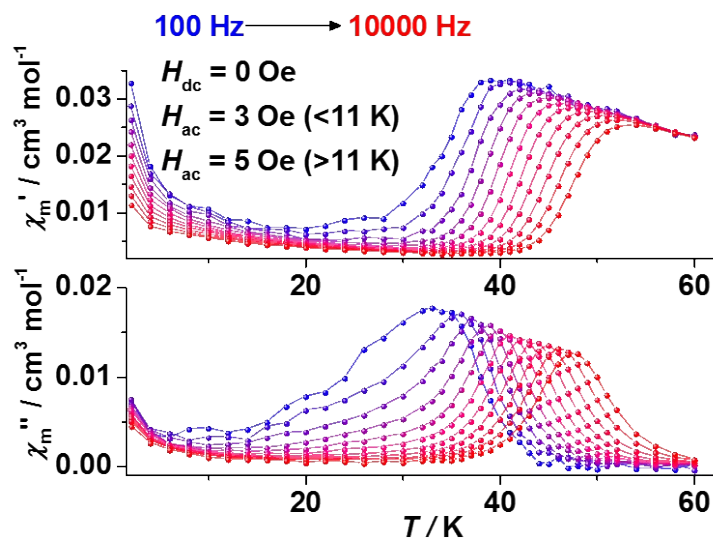


Figure S30. Plots of temperature dependent in-phase (χ') and out-of-phase (χ'') components of ac susceptibility (100~10000 Hz) of **3** under zero static field.

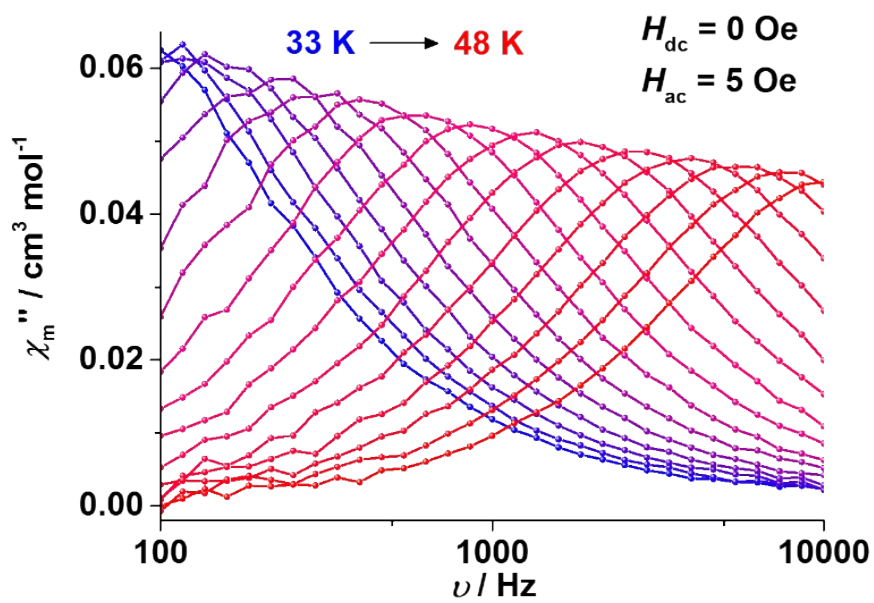


Figure S31. Plots of frequency dependent out-of-phase (χ'') component of ac susceptibility (100~10000 Hz) of **3** at zero static field.

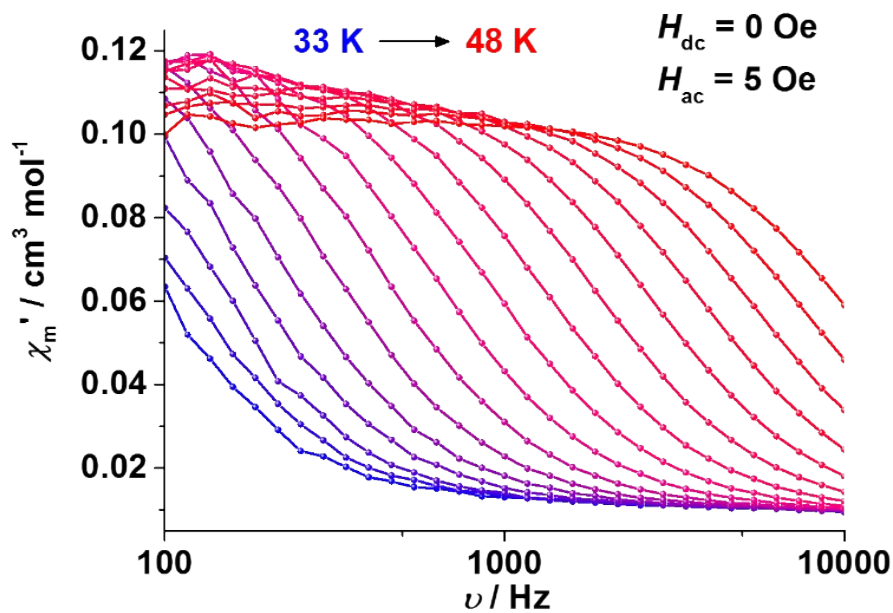


Figure S32. Plots of frequency dependent in-phase (χ') component of ac susceptibility (100~10000 Hz) of **3** at zero static field.

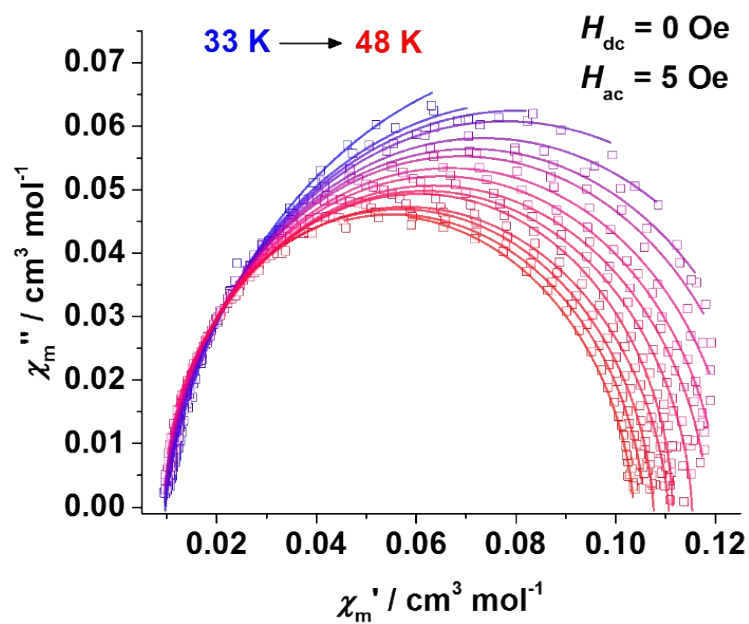


Figure S33. Argand plots of **3** between 33 K and 48 K from the data at Figure S25 at zero static field. .

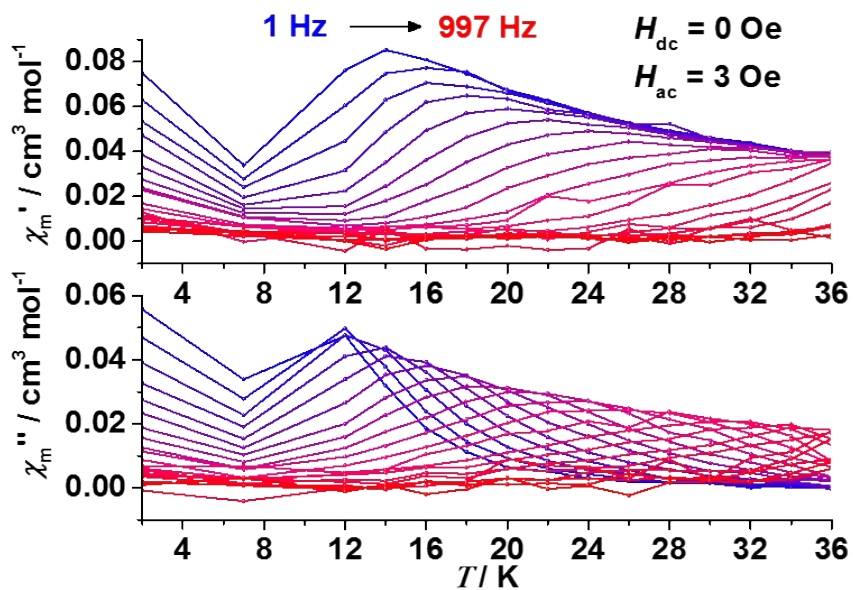


Figure S34. Plots of temperature dependent in-phase (χ') and out-of-phase (χ'') components of ac susceptibility (1~1000 Hz) of **3** at zero static field.

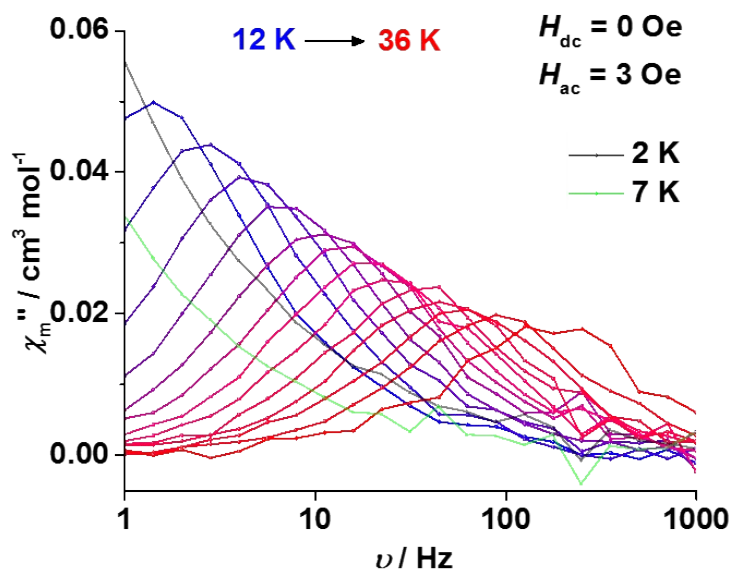


Figure S35. Plots of frequency dependent out-of-phase (χ'') component of ac susceptibility (1~1000 Hz) of **3** at zero static field.

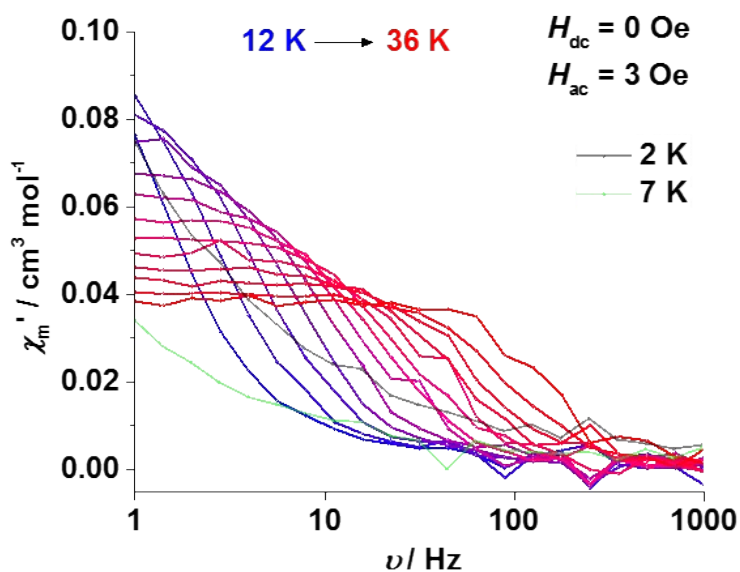


Figure S36. Plots of frequency dependent in-phase (χ') component of ac susceptibility (1~1000 Hz) of **3** at zero static field.

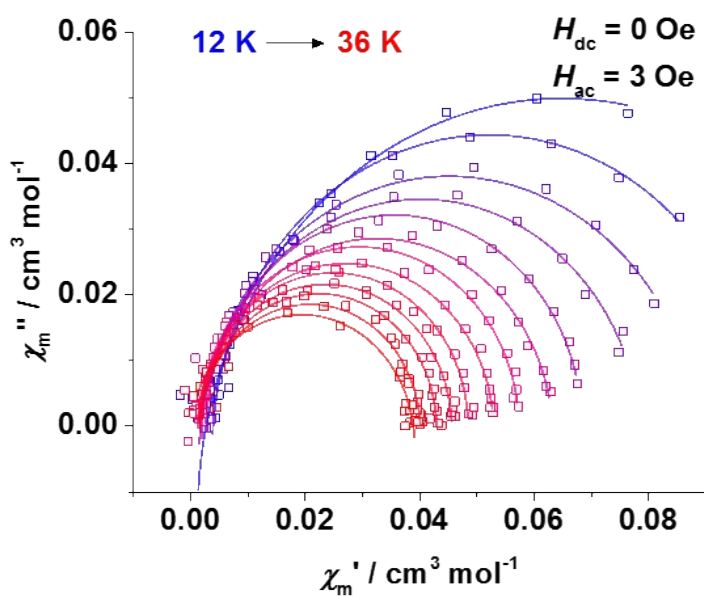


Figure S37. Argand plots of **3** between 12 K and 36 K from the data at Figure S29 at zero static field.

Table S5. Fitting parameters of **3** at zero static field.

Data corrected on MPMS (1~1000 Hz)				
Temperature (K)	χ_t (emu mol ⁻¹)	χ_s (emu mol ⁻¹)	α	τ (s)
12	0.00292	0.12724	0.14071	1.312E-01
14	0.00409	0.10055	0.05573	5.981E-02
16	0.00146	0.08937	0.09431	3.592E-02

18	0.00191	0.07899	0.07249	2.285E-02
20	0.00285	0.06869	0.01871	1.481E-02
22	0.00216	0.06347	0.0487	1.099E-02
24	0.00159	0.05762	0.02078	8.250E-03
26	0.00139	0.05318	0.03296	6.390E-03
28	0.00165	0.04867	0.00947	4.630E-03
30	0.00167	0.04582	0.01926	3.630E-03
32	0.00199	0.04314	0.01842	2.710E-03
34	0.00174	0.04031	0.03148	1.840E-03
36	0	0.03906	0.09567	9.994E-04
Data corrected on PPMS (100~10000 Hz)				
Temperature (K)	χ_r (emu mo l⁻¹)	χ_s (emu mol⁻¹)	α	τ (s)
33	0.17711	0.00983	0.10697	2.810E-03
34	0.15441	0.00992	0.08015	1.920E-03
35	0.15177	0.00956	0.08363	1.520E-03
36	0.14667	0.00954	0.0779	1.130E-03
37	0.13829	0.00944	0.06694	7.779E-04
38	0.13283	0.00938	0.05866	5.443E-04
39	0.12923	0.00935	0.0534	3.809E-04
40	0.12498	0.00904	0.05392	2.590E-04
41	0.12144	0.00889	0.05071	1.785E-04
42	0.11907	0.00825	0.05912	1.228E-04
43	0.11569	0.00848	0.04877	8.476E-05
44	0.11181	0.00975	0.02366	5.930E-05
45	0.11096	0.00565	0.07054	3.998E-05
46	0.10793	0.00614	0.05429	2.846E-05
47	0.10614	0.0053	0.05938	1.983E-05
48	0.10398	0.00291	0.06286	1.370E-05

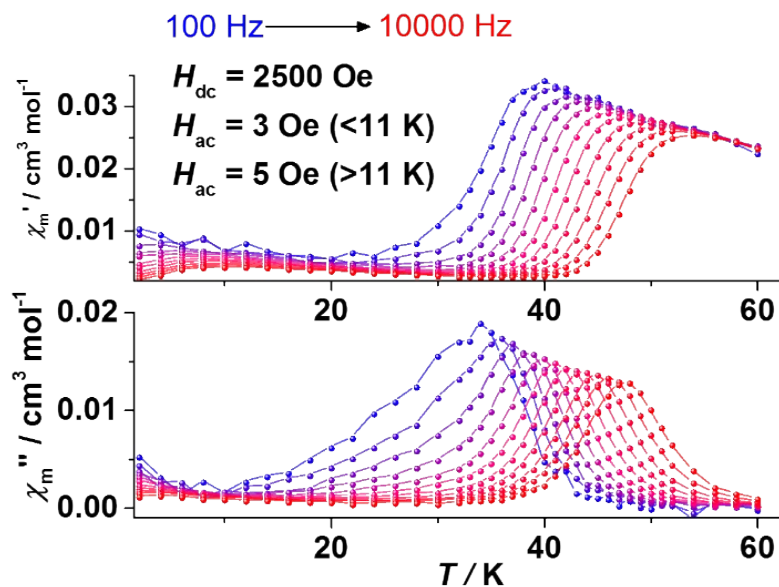


Figure S38. Plots of temperature dependent in-phase (χ') and out-of-phase (χ'') components of ac susceptibility (100~10000 Hz) of **3** at 2500 Oe static field.

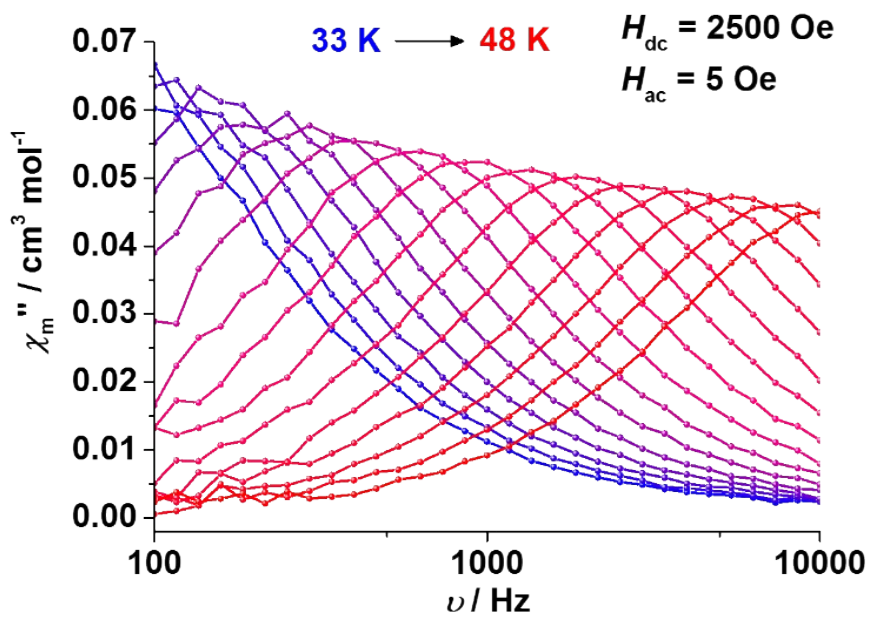


Figure S39. Plots of frequency dependent out-of-phase (χ'') component of ac susceptibility (100~10000 Hz) of **3** at 2500 Oe static field.

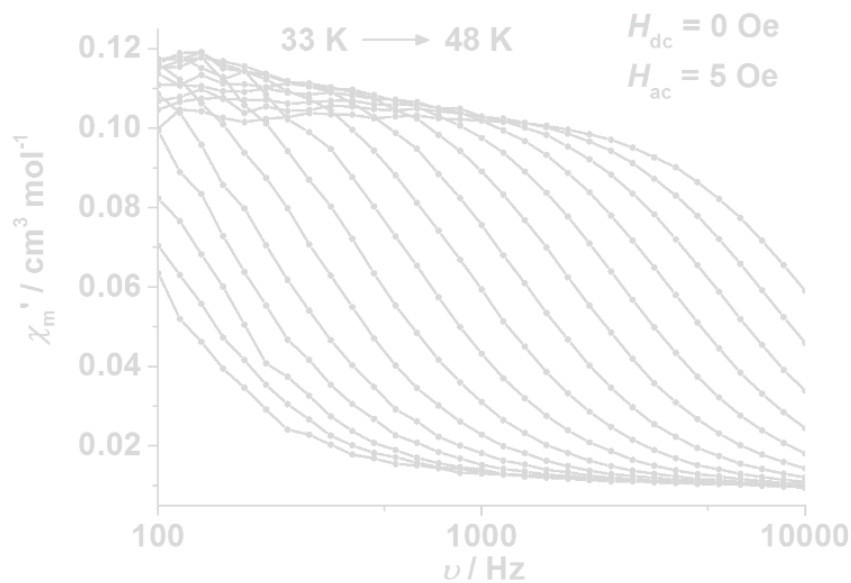


Figure S40. Plots of frequency dependent in-phase (χ') component of ac susceptibility (100~10000 Hz) of **3** at 2500 Oe static field.

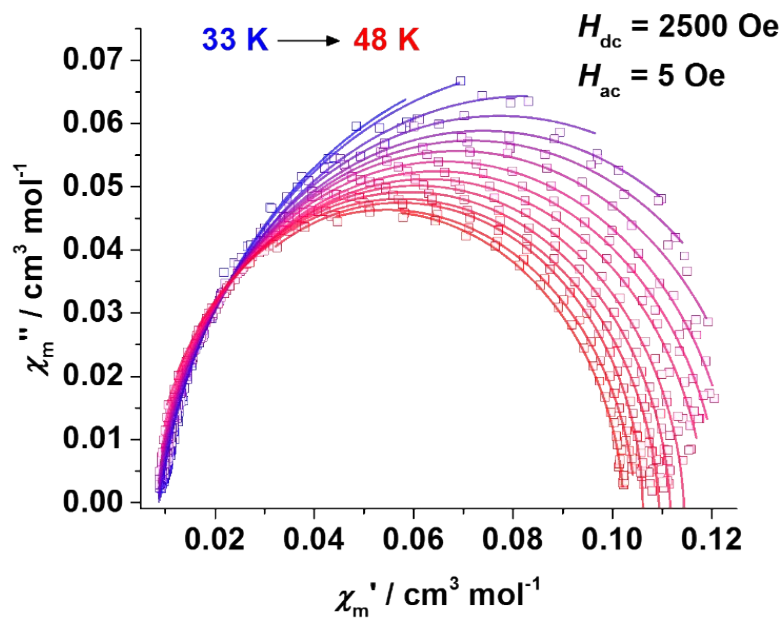


Figure S41. Argand plots of **3** between 33 K and 48 K from the data at Figure S33at 2500 Oe static field. .

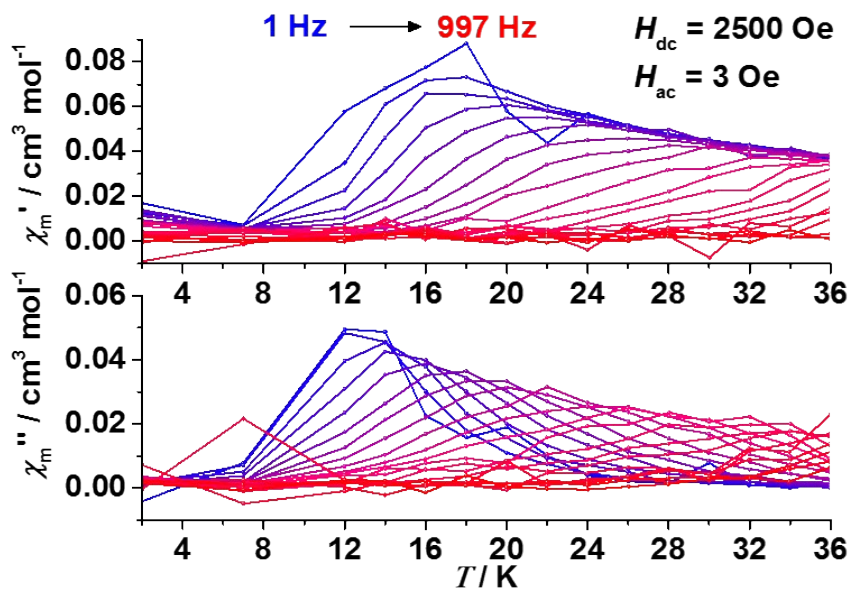


Figure S42. Plots of temperature dependent in-phase (χ') and out-of-phase (χ'') components of ac susceptibility (1~1000 Hz) of **3** at 2500 Oe static field.

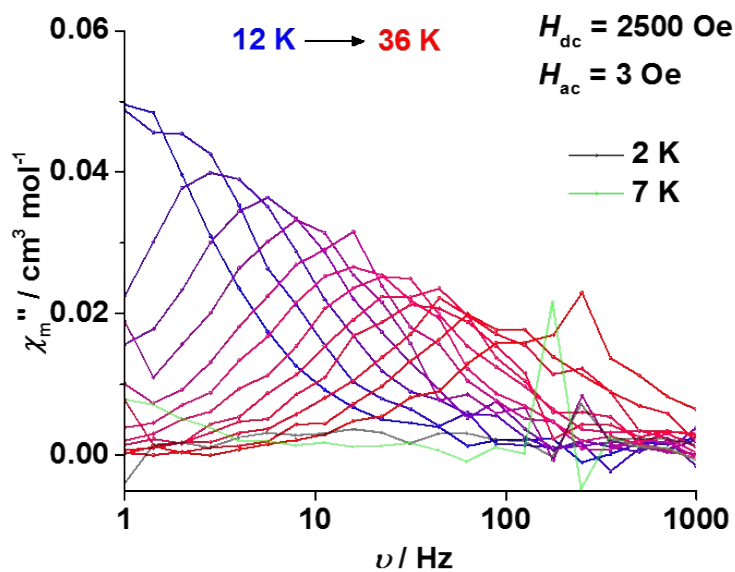


Figure S43. Plots of frequency dependent out-of-phase (χ'') component of ac susceptibility (1~1000 Hz) of **3** at 2500 Oe static field.

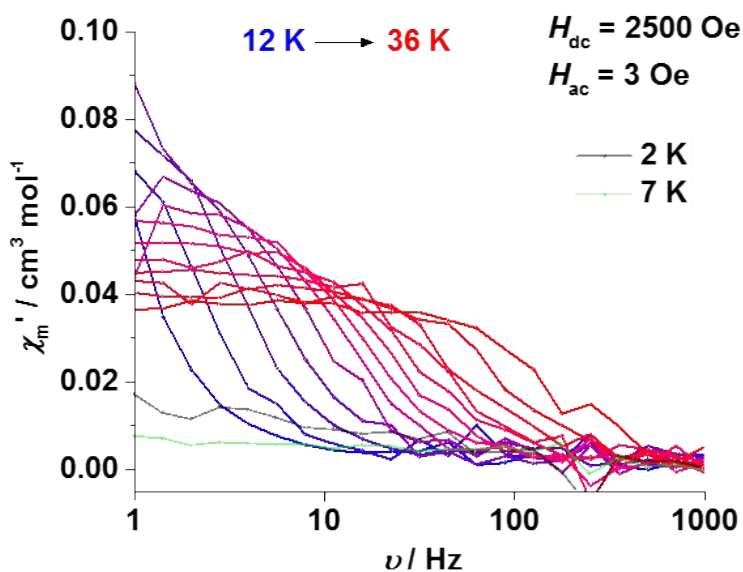


Figure S44. Plots of frequency dependent in-phase (χ') component of ac susceptibility (1~1000 Hz) of **3** at 2500 Oe static field.

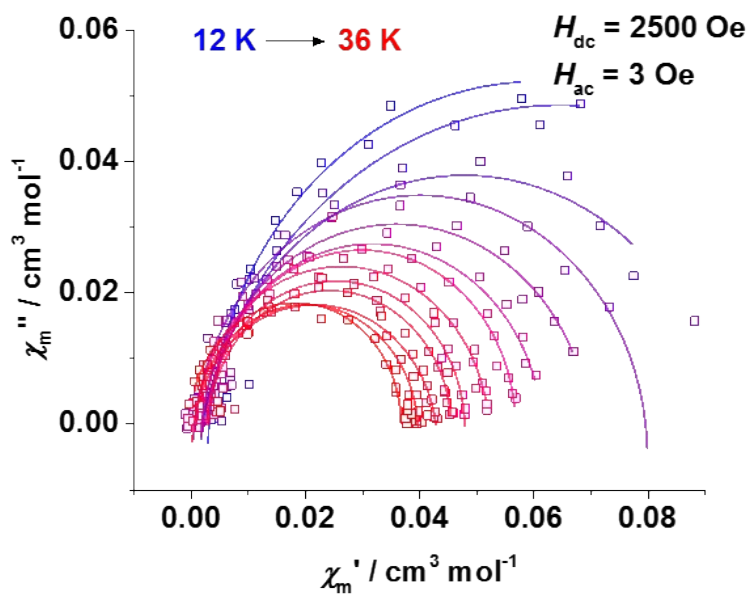


Figure S45. Argand plots of **3** between 12 K and 36 K from the data at Figure S37 at 2500 Oe static field.

Table S6. Fitting parameters of **3** at 2500 Oe static field.

Data corrected on MPMS (1~1000 Hz)				
Temperature (K)	χ_t (emu mol ⁻¹)	χ_s (emu mol ⁻¹)	α	τ (s)
14	0.00198	0.12755	0.16355	1.354E-01
16	0.0023	0.09377	0.12189	5.225E-02
18	8.21646E-4	0.07979	0.08251	3.008E-02

20	0.00201	0.07017	0.07528	2.148E-02
22	0.00212	0.06174	0.05675	1.357E-02
24	0.00323	0.057	0.01356	9.900E-03
26	8.7937E-4	0.05229	0.04847	7.000E-03
28	0.00289	0.04809	0.02841	5.160E-03
30	0.00315	0.04577	0.03552	4.530E-03
32	6.45322E-4	0.04302	0.10333	2.790E-03
34	6.46477E-4	0.03988	0.05451	1.930E-03
36	0	0.03694	0.00682	9.987E-04
Data corrected on PPMS (100~10000 Hz)				
Temperature (K)	χ_t (emu mo l⁻¹)	χ_s (emu mol⁻¹)	α	τ (s)
33	0.17303	0.00913	0.0973	2.880E-03
34	0.16981	0.00892	0.0998	2.330E-03
35	0.15743	0.00877	0.09296	1.670E-03
36	0.14633	0.00873	0.07579	1.130E-03
37	0.13996	0.0086	0.07131	8.029E-04
38	0.1355	0.00842	0.06749	5.646E-04
39	0.12965	0.00844	0.05592	3.856E-04
40	0.12502	0.00822	0.05198	2.595E-04
41	0.12219	0.00762	0.05814	1.788E-04
42	0.11915	0.00693	0.06034	1.232E-04
43	0.11473	0.00694	0.04783	8.480E-05
44	0.11195	0.00656	0.04657	5.778E-05
45	0.10967	0.00577	0.05173	4.043E-05
46	0.10647	0.00859	0.02199	2.965E-05
47	0.10496	0.00497	0.05082	2.002E-05
48	0.10261	0.00411	0.04529	1.427E-05

Table S7. Arrhenius fitting* parameters in Figure 5. (ZF=zero field; HF=2500 Oe dc field)

	1@ZF	1@HF	3@ZF	3@HF
U_{eff}/k_B (K)	721 ± 9	704 ± 10	721 ± 12	710 ± 10
τ_0 (s)	6.6×10 ⁻¹² , [exp(-25.74±0.19)]	6.1×10 ⁻¹² , [exp(-25.82±0.29)]	4.4×10 ⁻¹² , [exp(-26.15±0.26)]	5.6×10 ⁻¹² , [exp(-25.91±0.22)]
R^2	0.9990	0.9986	0.9981	0.9986

* The fitting equation is $\ln \left(\frac{\tau}{\tau_0} \right) = U_{eff}/k_B T - \ln(\tau_0/s)$.

Table S8. Dual process fitting* parameters in Figure 5. (ZF=zero field; HF=2500 Oe dc field)

	1@ZF	1@HF	3@ZF	3@HF
U_{eff}/k_B (K)	754 ± 8	763 ± 20	755 ± 13	759 ± 23
τ_0 (s)	3.5×10 ⁻¹² ± 6×10 ⁻¹³	2.6×10 ⁻¹² ± 1.2×10 ⁻¹²	2.1×10 ⁻¹² ± 6×10 ⁻¹³	2.0×10 ⁻¹² ± 1.1×10 ⁻¹²
C (s⁻¹ K⁻ⁿ)	2.7×10 ⁻⁴ ± 3×10 ⁻⁵	3.0×10 ⁻⁴ ± 9×10 ⁻⁵	8.3×10 ⁻⁴ ± 1.3×10 ⁻⁴	1.5×10 ⁻⁴ ± 5×10 ⁻⁵
n	4.00 ± 0.03	4.02 ± 0.09	3.74 ± 0.05	4.21 ± 0.11
R^2	0.9998	0.9986	0.9996	0.9985

*The fitting equation is $\ln \left(\frac{\tau}{\tau_0} \right) = - \ln \left(\left(\frac{1}{\tau_0} \exp \left(\frac{U_{eff}}{k_B T} \right) + C T^n \right) s \right)$.

IV. Ab initio Calculation

Method

The calculation fragment is built based on the molecule structure of complex **1**. All the *tert*-butyl groups were replaced by methyl groups. During the calculations, the other Dy^{III} ion was replaced by diamagnetic Lu^{III}. The basis sets for all atoms are atomic natural orbitals from the MOLCAS ANO-RCC library: ANO-RCC-VTZP for Dy^{III} ions; VTZ for close O; VDZ for distant atoms. The calculations employed the second order Douglas-Kroll-Hess Hamiltonian, where scalar relativistic contractions were taken into account in the basis set and the spin-orbit couplings were handled separately in the restricted active space state interaction (RASSI-SO) procedure. We have mixed the maximum number of spin-free state which was possible with our hardware (all from 21 sextets, 128 from 224 quadruplets, 130 from 490 doublets for the Dy^{III} fragment).

Result and discussion

According to a reported methodology⁴, the transition probability ratio is approximately proportional to $\exp(-E/k_B T) \bar{\mu}^2$, where E is the energy gap and $\bar{\mu}$ is the average value of magnetic moment matrix elements connecting opposite components of doublets. $\bar{\mu}$ values were shown in Figure S46 and Figure 4 respectively for CAS(9,7) and CAS(11,8). In the case of CAS(9,7), $P_{3^- \rightarrow 3^+} / P_{2^- \rightarrow 2^+} = 1.7$ with $T=50$ K, indicating that the TA-QTM process will occur through the second-excited states (KD 3 in Table S9). However, the corresponding energy gap is only 460.0 cm^{-1} , which is smaller than experimental U_{eff} . While in the case of CAS(11,8), although $P_{3^- \rightarrow 3^+} / P_{2^- \rightarrow 2^+} = 1.0$ with $T=50$ K, the corresponding $\bar{\mu}_{3^- \rightarrow 3^+} / \bar{\mu}_{2^- \rightarrow 2^+} = 17$. This means that the probability ratio will increase with T increase. That means the plots of $\ln \tau$ vs T^{-1} for the thermal relaxation process has not reached to the linear regime yet. If the temperature is higher, the TA-QTM will occur through the second excited states (KD 3). The corresponding energy gap is 528.3 cm^{-1} . This is coincided with the result of dual process fitting, in which the energy barrier of Orbach process is 524.3 cm^{-1} (754 K).

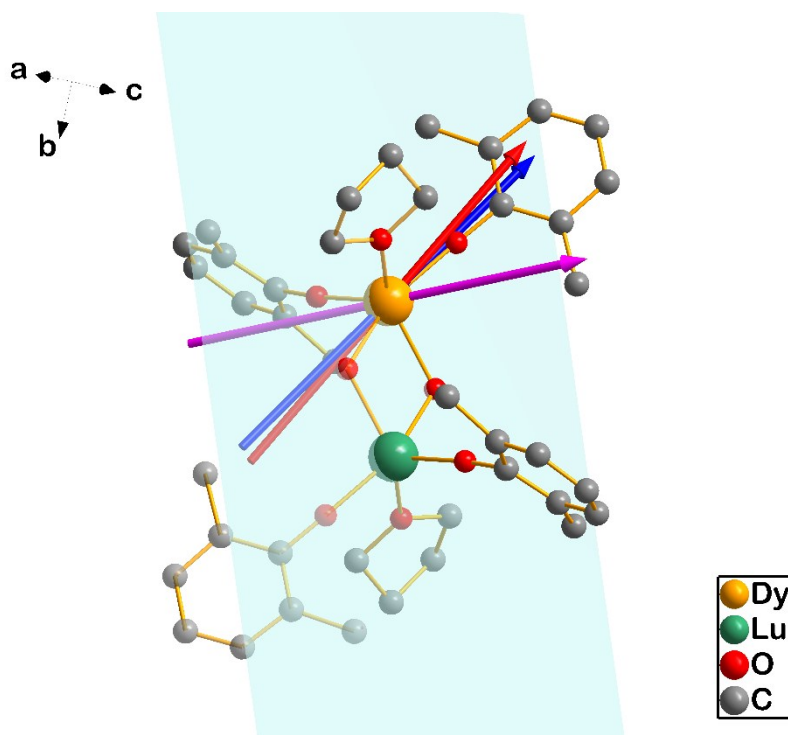


Figure S46. The fragment for the *ab initio* calculation (all H atom are omitted). Arrows show the directions of g_z vectors calculated by the method CAS(11,8) (blue for the ground doublets, red for first-excited doublets and pink for second-excited doublets).

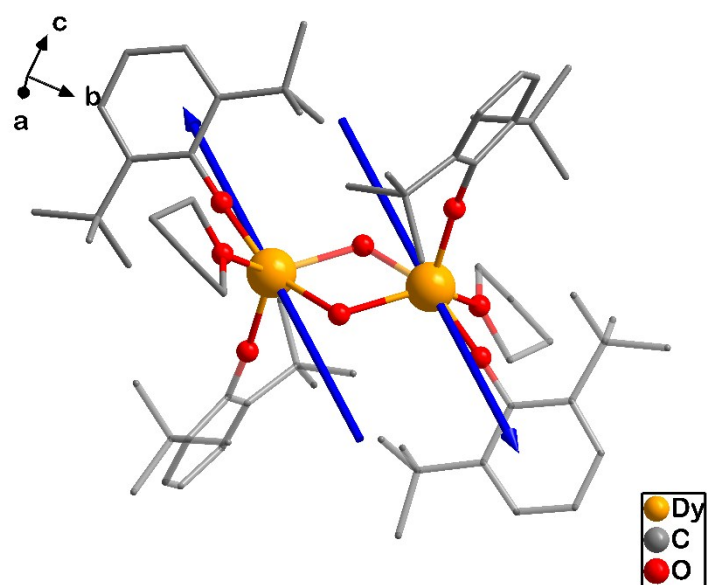


Figure S47. Orientations of the local main magnetizations (blue arrows) of the ground doublets on Dy^{III} ions of **1**.

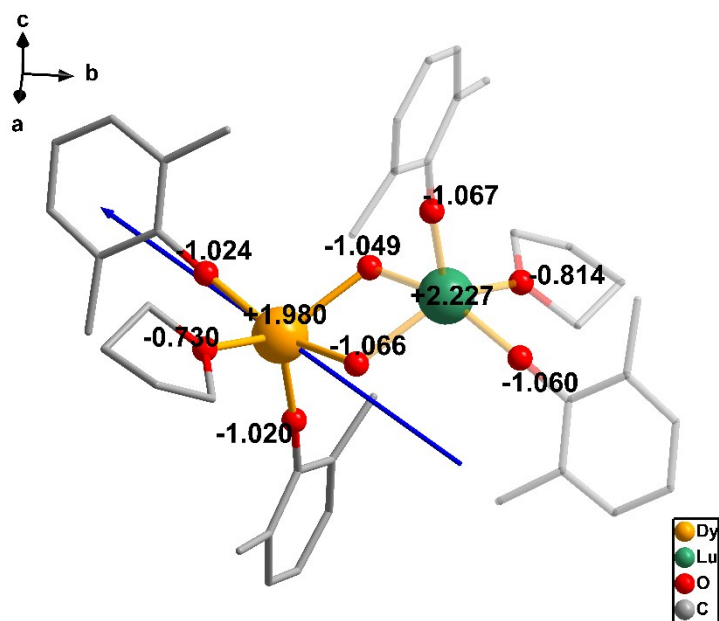


Figure S48. Mulliken charges on each atom center of Ln_2O_8 structure in the molecular fragment, blue arrow shows the easy axis of ground doublets.

Table S9. Relative energy ($E/k_B, K$) and effective g values ($\tilde{S} = \pm 1/2$) in xyz direction of the lowest 8 KDs obtained respectively from two kind of *ab initio* calculations of individual Dy^{III} fragment.

Kramers Doublets	CAS(9,7)					CAS(11,8)				
	E (cm ⁻¹)	E/k_B (K)	g_x	g_y	g_z	E (cm ⁻¹)	E/k_B (K)	g_x	g_y	g_z
1	0	0	0.001	0.001	19.831	0	0	0.002	0.002	19.856
2	309.6	445.5	0.081	0.133	16.755	331.9	477.5	0.090	0.108	17.121
3	460.0	661.8	0.861	1.159	15.464	528.3	760.1	1.306	2.151	12.596
4	537.7	773.6	0.410	2.289	10.079	605.8	871.6	0.091	3.774	11.258
5	619.1	890.8	7.618	6.022	3.204	656.2	944.1	0.724	2.336	13.912
6	664.4	955.9	1.981	4.009	14.342	707.8	1018.4	4.257	5.446	9.703
7	740.2	1065.0	0.102	0.211	16.623	808.7	1163.6	1.301	2.273	15.520
8	899.5	1294.2	0.024	0.032	19.255	905.6	1303.0	0.413	0.930	18.649

Table S10. *Ab initio* calculation based composition for the wave functions (wf1 to wf16) corresponding to the 8 Kramers doublets of the ⁶H_{15/2} multiplet in wave functions with definite projection of the total moment |JM>, together with the angle between main axes of corresponding state doublets and the ground state doublets.

CAS(9,7)																
Doublets	1		2		3		4		5		6		7		8	
E (cm ⁻¹)	0		309.6		460		537.7		619.1		664.4		740.2		899.5	
Angle(°)	0		5.5		55.3		29.7		29.3		79.8		78.9		65.9	
	wf1	wf2	wf3	wf4	wf5	wf6	wf7	wf8	wf9	wf10	wf11	wf12	wf13	wf14	wf15	wf16
⁻ 15/2>	0.99	0.00	0.00	0.00	0.00	0.00	0.00	0.00	0.00	0.00	0.00	0.00	0.00	0.00	0.00	0.00
⁻ 13/2>	0.00	0.00	0.93	0.00	0.00	0.01	0.02	0.00	0.00	0.02	0.00	0.00	0.01	0.00	0.00	0.01
⁻ 11/2>	0.00	0.00	0.01	0.00	0.00	0.33	0.44	0.01	0.01	0.01	0.03	0.02	0.06	0.01	0.00	0.05
⁻ 9/2>	0.00	0.00	0.03	0.00	0.00	0.08	0.11	0.01	0.03	0.28	0.09	0.01	0.17	0.01	0.00	0.18
⁻ 7/2>	0.00	0.00	0.01	0.00	0.00	0.14	0.02	0.01	0.02	0.18	0.15	0.05	0.06	0.05	0.01	0.29
⁻ 5/2>	0.00	0.00	0.00	0.00	0.00	0.17	0.03	0.00	0.05	0.04	0.12	0.25	0.00	0.06	0.00	0.26
⁻ 3/2>	0.00	0.00	0.00	0.00	0.01	0.12	0.08	0.07	0.10	0.02	0.11	0.11	0.20	0.04	0.01	0.12
⁻ 1/2>	0.00	0.00	0.00	0.00	0.03	0.10	0.15	0.04	0.12	0.12	0.01	0.03	0.12	0.22	0.01	0.05
1/2>	0.00	0.00	0.00	0.00	0.10	0.03	0.04	0.15	0.12	0.12	0.03	0.01	0.22	0.12	0.05	0.01
3/2>	0.00	0.00	0.00	0.00	0.12	0.01	0.07	0.08	0.02	0.10	0.11	0.11	0.04	0.20	0.12	0.01
5/2>	0.00	0.00	0.00	0.00	0.17	0.00	0.00	0.03	0.04	0.05	0.25	0.12	0.06	0.00	0.26	0.00
7/2>	0.00	0.00	0.00	0.01	0.14	0.00	0.01	0.02	0.18	0.02	0.05	0.15	0.05	0.06	0.29	0.01
9/2>	0.00	0.00	0.00	0.03	0.08	0.00	0.01	0.11	0.28	0.03	0.01	0.09	0.01	0.17	0.18	0.00
11/2>	0.00	0.00	0.00	0.01	0.33	0.00	0.01	0.44	0.01	0.01	0.02	0.03	0.01	0.06	0.05	0.00
13/2>	0.00	0.00	0.00	0.93	0.01	0.00	0.00	0.02	0.02	0.00	0.00	0.00	0.00	0.01	0.01	0.00
15/2>	0.00	0.99	0.00	0.00	0.00	0.00	0.00	0.00	0.00	0.00	0.00	0.00	0.00	0.00	0.00	0.00

CAS(11,8)																
Doublets	1		2		3		4		5		6		7		8	
E (cm ⁻¹)	0		331.9		528.3		605.8		656.2		707.8		808.7		905.6	
Angle(°)	0.0		14.0		14.4		56.1		76.7		80.9		87.3		65.5	
	wf1	wf2	wf3	wf4	wf5	wf6	wf7	wf8	wf9	wf10	wf11	wf12	wf13	wf14	wf15	wf16

-15/2 >	1.00	0.00	0.00	0.00	0.00	0.00	0.00	0.00	0.00	0.00	0.00	0.00	0.00
-13/2 >	0.00	0.00	0.90	0.00	0.06	0.00	0.02	0.00	0.00	0.00	0.00	0.00	0.01
-11/2 >	0.00	0.00	0.06	0.00	0.60	0.00	0.01	0.01	0.10	0.00	0.05	0.06	0.03
-9/2 >	0.00	0.00	0.02	0.00	0.12	0.00	0.21	0.07	0.01	0.07	0.08	0.09	0.13
-7/2 >	0.00	0.00	0.00	0.00	0.08	0.00	0.17	0.02	0.07	0.07	0.09	0.10	0.01
-5/2 >	0.00	0.00	0.00	0.00	0.03	0.00	0.09	0.00	0.34	0.05	0.02	0.10	0.12
-3/2 >	0.00	0.00	0.01	0.00	0.01	0.00	0.23	0.00	0.07	0.02	0.16	0.13	0.15
-1/2 >	0.00	0.00	0.00	0.00	0.08	0.01	0.03	0.13	0.17	0.04	0.09	0.02	0.09
1/2 >	0.00	0.00	0.00	0.00	0.01	0.08	0.13	0.03	0.04	0.17	0.02	0.09	0.28
3/2 >	0.00	0.00	0.00	0.01	0.00	0.01	0.00	0.23	0.02	0.07	0.13	0.16	0.05
5/2 >	0.00	0.00	0.00	0.00	0.00	0.03	0.00	0.09	0.05	0.34	0.10	0.02	0.00
7/2 >	0.00	0.00	0.00	0.00	0.00	0.08	0.02	0.17	0.07	0.07	0.10	0.09	0.14
9/2 >	0.00	0.00	0.00	0.02	0.00	0.12	0.07	0.21	0.07	0.01	0.09	0.08	0.00
11/2 >	0.00	0.00	0.00	0.06	0.00	0.60	0.01	0.01	0.00	0.10	0.06	0.05	0.01
13/2 >	0.00	0.00	0.00	0.90	0.00	0.06	0.00	0.02	0.00	0.00	0.00	0.00	0.00
15/2 >	0.00	1.00	0.00	0.00	0.00	0.00	0.00	0.00	0.00	0.00	0.00	0.00	0.00

V. Magnetic interaction analysis

Compound 1

The dipole-dipole interaction between two sites can be described with Hamiltonian in Equation (S1). The tensor can be obtained with Equation (S2) in cgs expression, where \vec{g}_i is the g tensor of the dipole at site i , \vec{r} is the unit vector at the direction from site i to site j , $|r|$ is the length between the two sites. Under Ising approximation, Equation (S2) could be expressed as Equation (S3), where the \vec{g}_{iz} is the vector of the dipole at site i , which could be calculated using the program *SINGLE_ANISO* with the results of *ab initio* calculations. For inverted dimer, Equation (S3) can be simplified as Equation (S4), where θ is the angle between main magnetization axis and \vec{r} vector ($\theta \in [0, 90^\circ]$). In this paper, we just used the \vec{g}_z vector obtained using *SINGLE_ANISO* directly ($S_{Dy} = \pm 1/2$), and obtained $J_{dip} = 1.8 \text{ cm}^{-1}$, ferromagnetically.

$$\hat{H}_{dip} = \vec{S}_1 \cdot \vec{J}_{dip} \cdot \vec{S}_2 \quad (\text{S1})$$

$$\vec{J}_{dip} = \frac{\mu_B^2}{|r|^3} [\vec{g}_1 \cdot \vec{g}_2 - 3(\vec{g}_1 \cdot \vec{r})(\vec{r} \cdot \vec{g}_2)] \quad (\text{S2})$$

$$J_{dip} = \frac{\mu_B^2}{|r|^3} [g_{1z} \cdot g_{2z} - 3(g_{1z} \cdot \vec{r})(\vec{r} \cdot g_{2z})] \quad (\text{S3})$$

$$J_{dip} = \frac{\mu_B^2}{|r|^3} g_{1z} \cdot g_{2z} (1 - 3\cos^2\theta) \quad (\text{S4})$$

We took two steps to fit the exchange interaction in compound 1. Firstly, we calculated the

mononuclear fragments using CASSCF to obtain the corresponding magnetic properties (*vide infra*). And then, the exchange interaction between the magnetic centers is considered within the Lines model, while the account of the dipole-dipole magnetic coupling is treated exactly.

The exchange Hamiltonian is:

$$H_{\text{exch}} = -J_{\text{Dy-Dy}}^{\text{total}} \hat{S}_{\text{Dy}1} \hat{S}_{\text{Dy}2} \quad (\text{S4})$$

The $J_{\text{Dy-Dy}}^{\text{total}}$ is parameter of the total magnetic interaction ($J^{\text{total}} = J^{\text{dipolar}} + J^{\text{exchange}}$) between magnetic center ions. The $\hat{S}_{\text{Dy}} = \pm 1/2$ is the ground pseudospin on the Dy site. The dipolar magnetic coupling can be calculated exactly, while the exchange coupling constants were fitted through comparison of the computed and measured magnetic susceptibility using the *POLY_ANISO* program⁵. The intermolecular interaction zJ' of **1** was set to 0.01 cm⁻¹.

Table S11. Calculated energies (cm⁻¹), the corresponding tunneling gaps (cm⁻¹) and the g_z values of the low-lying exchange doublet states of complex **1**.

1		
E	Δ_{tun}	g_z
0.00	0.91 E-15	0.000
1.69	0.11 E-13	39.663

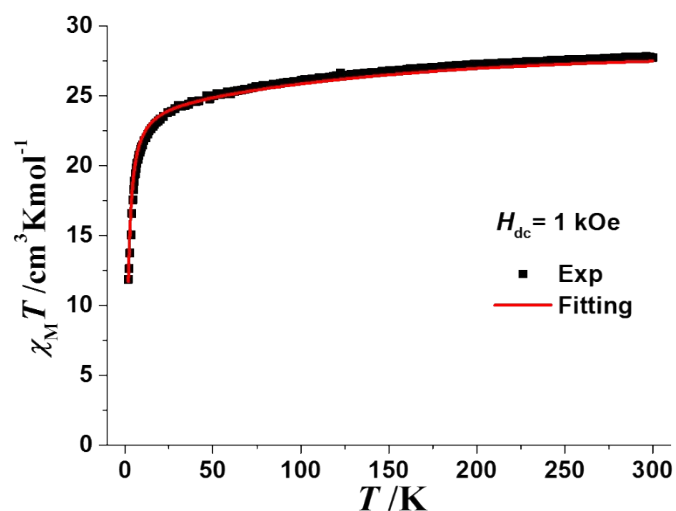


Figure S49. A comparison of the experimental (black dots) and calculated (red solid line) magnetic susceptibility using *POLY_ANISO* for complex **1**.

Compound 4

For Gd^{III} dimers, an isotropic magnetic interaction model is usually employed. Analytical method is based on van Vleck equation and Kambe's vector schemes. For Gd^{III} ($S = 7/2$, $g = 2.0$), Eq(S5)⁶ is used for fitting. We used least square method and obtained $J_{\text{iso}}(\text{Gd}^{\text{III}}-\text{Gd}^{\text{III}}) = -0.219 \pm 0.002 \text{ cm}^{-1}$, $R^2=0.989$. When g was relaxed as fitting parameters, the fitting gave $J_{\text{iso}}(\text{Gd}^{\text{III}}-\text{Gd}^{\text{III}}) = -0.231 \pm 0.000 \text{ cm}^{-1}$, $g = 2.01 \pm 0.00$ and $R^2=1.000$.

$$\chi_m T = \frac{2Ng^2\beta^2}{k} \frac{e^{J/kT} + 5e^{3J/kT} + 14e^{6J/kT} + 30e^{10J/kT} + 55e^{15J/kT} + 91e^{21J/kT} + 140e^{28J/kT}}{1 + 3e^{J/kT} + 5e^{3J/kT} + 7e^{6J/kT} + 9e^{10J/kT} + 11e^{15J/kT} + 13e^{21J/kT} + 15e^{28J/kT}} \quad (\text{S5})$$

In compound **4**, the magnetic coupling showed obvious effect on the susceptibility mainly at low temperature. We also applied *PHI 2.1.6* program⁷ to fit the susceptibility numerically. At the beginning, we fixed *g* value to 2.0, and obtained $J_{\text{iso}}(\text{Gd}^{\text{III}}-\text{Gd}^{\text{III}}) = -0.22 \text{ cm}^{-1}$. To get a better fit to the susceptibility curves, *g* value was relaxed and produced $J_{\text{iso}}(\text{Gd}^{\text{III}}-\text{Gd}^{\text{III}}) = -0.23 \text{ cm}^{-1}$, $g = 2.01$.

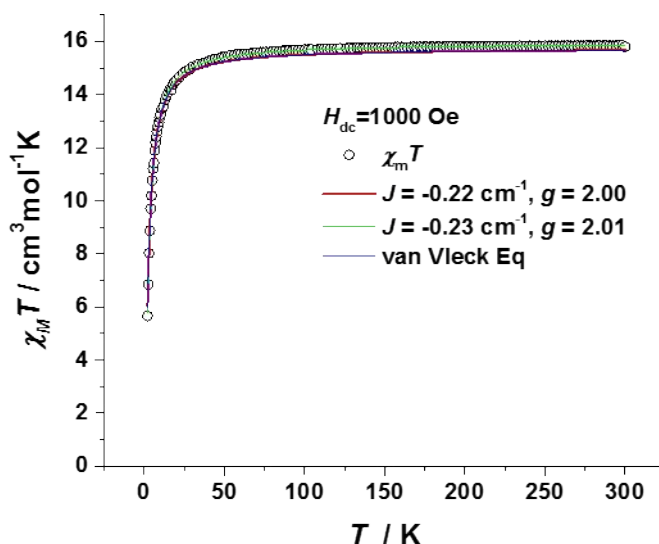


Figure S50. A comparison of the experimental (black dots) and calculated (line) magnetic susceptibility for complex **4**. The red and green line were obtained using numerical method, the blue line was obtained using van Vleck equation.

Reference

1. D. C. Bradley, J. S. Ghotra and F. A. Hart, *Journal of the Chemical Society, Chemical Communications*, 1972, DOI: 10.1039/c39720000349, 349.
2. Sheldrick, G. M. *SHELXL-97*; University of Göttingen: Göttingen, Germany, 1997.
3. a) J. Cirera, E. Ruiz, S. Alvarez, *Chem. Eur. J.*, **2006**, *12*, 3162-3167; b) M. Pinsky, D. Avnir, *Inorg. Chem.* **1998**, *37*, 5575-5582; c) D. Casanova, J. Cirera, M. Llunell, P. Alemany, D. Avnir, S. Alvarez, *J. Am. Chem. Soc.*, **2004**, *126*, 1755-1763.
4. L. Ungur, M. Thewissen, J. P. Costes, W. Wernsdorfer, L. F. Chibotaru, *Inorg. Chem.* **2013**, *52*, 6328-6337.
5. a) L. F. Chibotaru, L. Ungur, A. Soncini, *Angew. Chem. Int. Ed.*, **2008**, *47*, 4126-4129; b) L. Ungur, W. Van den Heuvel, L. F. Chibotaru, *New J. Chem.*, **2009**, *33*, 1224-1230; c) L. F. Chibotaru, L. Ungur, C. Aronica, H. Elmolli, G. Pilet, D. Luneau, *J. Am. Chem. Soc.*, **2008**, *130*, 12445-12455.
6. F. Pointillart, Y. Le Gal, S. Golhen, O. Cador, L. Ouahab, *Chem. Eur. J.* **2011**, *17*, 10397-10404.

7. N. F. Chilton, R. P. Anderson, L. D. Turner, A. Soncini, K. S. Murray, *J. Comput. Chem.*, **2013**, *34*, 1164-1175.